A Comparison of Beamforming and Direction Finding Algorithms (Beamscan and MUSIC) on a Linear Array HF Radar in a Medium to Low Wave Energy Environment

DOUGLAS CAHL,[a] GEORGE VOULGARIS,[a] AND LYNN LEONARD[b]

[a] *School of the Earth, Ocean, and Environment, University of South Carolina, Columbia, South Carolina*
[b] *Department of Earth and Ocean Sciences, University of North Carolina, Wilmington, North Carolina*

(Manuscript received 13 January 2022, in final form 21 October 2022)

ABSTRACT: We assess the performance of three different algorithms for estimating surface ocean currents from two linear array HF radar systems. The delay-and-sum beamforming algorithm, commonly used with beamforming systems, is compared with two direction-finding algorithms: Multiple Signal Classification (MUSIC) and direction finding using beamforming (Beamscan). A 7-month dataset from two HF radar sites (CSW and GTN) on Long Bay, South Carolina (United States), is used to compare the different methods. The comparison is carried out on three locations (midpoint along the baseline and two locations with in situ Eulerian current data available) representing different steering angles. Beamforming produces surface current data that show high correlation near the radar boresight ($R^2 \geq 0.79$). At partially sheltered locations far from the radar boresight directions (59° and 48° for radar sites CSW and GTN, respectively) there is no correlation for CSW ($R^2 = 0$) and the correlation is reduced significantly for GTN ($R^2 = 0.29$). Beamscan performs similarly near the radar boresight ($R^2 = 0.8$ and 0.85 for CSW and GTN, respectively) but better than beamforming far from the radar boresight ($R^2 = 0.52$ and 0.32 for CSW and GTN, respectively). MUSIC's performance, after significant tuning, is similar near the boresight ($R^2 = 0.78$ and 0.84 for CSW and GTN) while worse than Beamscan but better than beamforming far from the boresight ($R^2 = 0.42$ and 0.27 for CSW and GTN, respectively). Comparisons at the midpoint (baseline comparison) show the largest performance difference between methods. Beamforming ($R^2 = 0.01$) is the worst performer, followed by MUSIC ($R^2 = 0.37$) while Beamscan ($R^2 = 0.76$) performs best.

KEYWORDS: In situ oceanic observations; Radars/Radar observations; Remote sensing

1. Introduction

Modern, land-based high-frequency (HF) radar systems are widely used to measure coastal surface ocean currents for both ocean research (e.g., Paduan and Shulman 2004) and operations (e.g., Harlan et al. 2010; Roarty et al. 2019). Their accuracy in measuring ocean currents has increased over the last few decades, mostly due to improvements in signal analysis and calibration methods (e.g., Barrick and Lipa 1999; Gurgel et al. 1999a; Kohut and Glenn 2003; Guérin et al. 2021). HF radar derived surface current measurements are utilized for improving numerical circulation model predictions (Paduan and Shulman 2004; Couvelard et al. 2021) through data assimilation. This has been shown to improve predictions relevant to oil spill response (Abascal et al. 2009) and search and rescue (Harlan et al. 2011; Bellomo et al. 2015) operations.

Surface current estimations are derived from the backscattered radar signal from ocean waves with a wavelength half that of the transmitted electromagnetic wavelength (Bragg scattering), first discovered by Crombie (1955). The difference between the HF radar measured speed of the Bragg wave and the theoretical one for still water is used to estimate the surface ocean current, toward or away from the radar site (Barrick and Weber 1977). The theoretical range resolution $\Delta r \approx c/(2B)$ of the HF radar system is determined by the bandwidth (B) of the radar (e.g., Gurgel et al. 1999b) and the speed of light c. Angular resolution is based on both the radar system (i.e., number of antennas and antenna array characteristics) as well as the signal processing method used. Most modern HF radar systems are mainly beamforming linear arrays (BLA; e.g., Gurgel et al. 1999a) or direction finding (DF) compact cross loop (CCL) systems (Barrick and Lipa 1997), called DF-CCL systems herein, although other configurations have been also used (e.g., Fernandez and Paduan 1996; Kirincich et al. 2019).

In modern monostatic BLA systems, the radar signal is transmitted toward the ocean, which is then backscattered from Bragg waves in the ocean that are traveling directly toward or away from the radar. The radar signal is backscattered from many locations in the ocean, which is then received by the receiving antennas. The signals from all the receive antennas are first range gated, separating the signal into different range bins. After this, each range bin is processed separately. The signal from all receiving antennas from a single range bin is digitally beamformed by summing the signal of individual antennas after applying a delay (phase shift) and an amplitude weight to them (e.g., Van Trees 2004). The phase shifts are chosen to maximize the array's sensitivity to incoming signal from a particular direction. The Bragg peaks in the resulting Doppler spectrum, for a particular direction and at a specific range, are then analyzed. The local maxima of the Bragg peaks are used to calculate their frequency (Doppler) shift from their still-water locations, which is due to the presence of a surface ocean current (Gurgel et al. 1999a).

DF uses the Doppler spectrum from each antenna to identify which Doppler frequencies (each corresponding to a different surface current velocity) correspond to Bragg scattering. Then, for each Doppler frequency identified, the bearing angle(s) of

Corresponding author: Douglas Cahl, dcahl@geol.sc.edu

DOI: 10.1175/JTECH-D-22-0005.1

the signal(s) is calculated using a direction-finding algorithm. The most common and successful direction-finding algorithm used with HF radars is the Multiple Signal Identification and Classification (MUSIC) first introduced by Schmidt (1986) and applied to HF radars by Barrick and Lipa (1997). Both BLA and DF-CCL radar systems provide reliable surface ocean currents (Essen et al. 2000) and offer similar levels of accuracy (Chapman et al. 1997; Kuang et al. 2012; Liu et al. 2014; Paduan and Washburn 2013). Although BLA systems require antenna arrays that are significantly larger than CCL systems, with 12–16 receive antennas they only offer 120° of coverage, ±60° from the boresight (perpendicular to the linear array) of the radar receiving array (Gurgel et al. 1999a) as opposed to 360° coverage for CCL systems (Barrick and Lipa 1997; Lai et al. 2017). With an 8-antenna linear array, the coverage is reduced to 90° or ±45° from the boresight.

Beamforming suppresses signals from other directions significantly better near the boresight than far from it. If the oceanic wave field is directed mainly along the boresight of the radar, the resulting radar signal is strongest along this direction and weaker at higher angles, with a minimum at 90° to the boresight. Under such conditions, when beamforming ("looking") far from the boresight the signal at 0° may not be sufficiently suppressed (Laws et al. 2000) leading to inaccuracies in current estimations. However, it has been argued theoretically, that when antenna patterns are ideal, beamforming is effective even under these conditions (Heron 2017), while others have suggested that using MUSIC on a linear array could outperform beamforming in this situation (Laws et al. 2000). The experimental study of Wang and Gill (2016) suggested that combining beamforming and MUSIC may offer the best surface ocean current estimates with a BLA radar system.

The objective of this study is to explore the possible benefits of using direction finding algorithms on a BLA radar system. The linear receiving array in BLA systems is commonly spaced by 0.45–0.5 radar wavelengths, where 0.5 is the optimal spacing for linear arrays using beamforming as well as MUSIC (Gupta and Kar 2015). In addition to MUSIC, one can simply use beamforming as the direction finding algorithm, where instead of analyzing the Doppler spectrum at each direction, the beam is scanned over azimuth for each frequency (e.g., Krim and Viberg 1996) corresponding to Bragg scattering. The direction where the power of this frequency is maximized is considered the direction of arrival (DOA) of that frequency. This direction finding method of beamforming has more recently been referred to as Beamscan in MATLAB's Phased Array System Toolbox (MathWorks 2022). In this manuscript the term "beamforming" refers to the method of analyzing the Doppler spectrum at each direction of interest, which is the default methodology for beamforming commercial HF radar systems such as Wellen radars (WERA) (Gurgel et al. 1999a). The term "Beamscan" refers to the method whereby beamforming is used as a direction finding method to create a spatial spectrum over direction for each frequency.

Although Beamscan has been compared with other direction finding methods in signal analysis research (e.g., Sun et al. 2018), to the authors' knowledge, it has not been used for HF radar surface current measurements. Degradation of beamforming performance at high steering angles (>50°) motivates the assessment of the algorithms (i.e., beamforming, Beamscan, and MUSIC) examined in this study at such high angles. It is worth noting that application of these methods depends on antenna geometry. While MUSIC can be applied to any antenna geometry, beamforming and Beamscan require a larger array, although theoretically you could apply beamforming to any antenna geometry as well. Such arrays commonly consist of 8–16 antennas spaced roughly half a wavelength apart on a linear configuration although other array geometries such as curved and circular arrays have also been used for beamforming. However, receiving arrays consisting of collocated antenna elements or very small grid arrays (less than wavelength in size) are not capable of beamforming well enough for use in HF radar surface current measurements.

In the remainder of the paper, we first present a brief description of the three methods (section 2). This is followed by a presentation (section 3) of the HF radar system and the in situ datasets used in this study. In section 4 the radial current estimates from each method are compared against the in situ data and against each HF radar system at a location along their baseline. Finally, the performance of the three methods is discussed in section 5 and the conclusions are presented in section 6.

2. HF radar surface current estimation methodology

a. *Initial signal processing and range sorting*

Gurgel et al. (1999b) have provided detail description of the signal processing applied in BLA radar systems; therefore, only a brief description is presented in here.

An HF radar emits an upward (or downward) frequency-modulated "chirp" signal, which is backscattered by the ocean waves and received by the system antennas. The individual antenna received signals are demodulated and recorded as a complex time series representing the in-phase (I) and quadrature-phase (Q) components. Then, an initial fast Fourier transform (FFT) is performed on the complex signal for each chirp i to estimate its energy distribution in the frequency domain:

$$G_i(f) = \mathrm{FFT}[I_i(t) + iQ_i(t)], \tag{1}$$

where t is the time within the chirp i (i.e., $t_i < t < t_i + T$ where T is the chirp duration and t_i is the starting time of chirp i). Because the transmit signal is "chirping" over a frequency range defined by the chirp bandwidth (B), the frequency bands from this FFT analysis correspond to different time delays, $[\Delta t = (T/B)f]$, which represent corresponding range bins $[r = (c\Delta t)/2 = (cTf)/(2B)$, where c is the speed of light in vacuum]. Using the above relationships, the signal for each chirp $[G_i(f)]$ is sorted into the different ranges it originated from $[G_i(r)]$.

Theoretically, the range resolution $[\Delta r = c/(2B)]$ is defined by the bandwidth of the chirp but the actual (effective) resolution is lower as it is affected by the window applied to the signal prior to applying the FFT (Voulgaris et al. 2011). Each

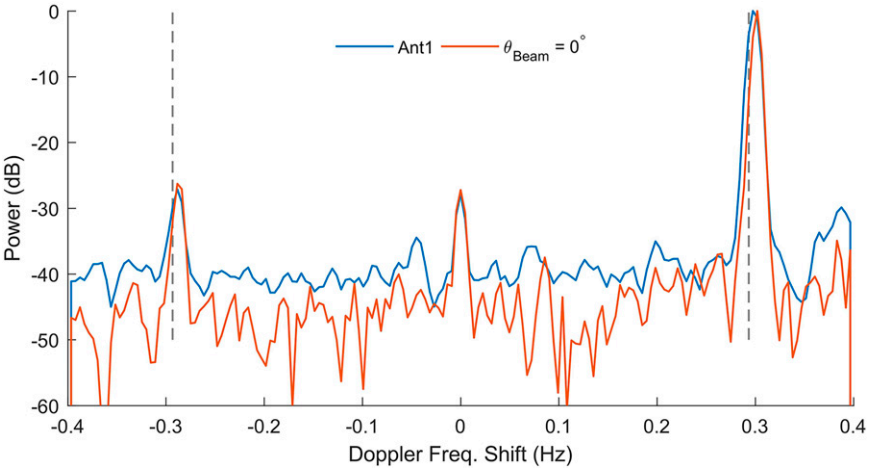

FIG. 1. Example of Doppler spectra from an 8.3 MHz radar for a single range cell (r = 30 km) from a single antenna (blue line) and from all 12 antennas beamformed along the boresight (red line). The location of the Bragg peaks in still water (theoretical) are shown as vertical dashed gray lines. The radar acquisition is 2048 chirps each with a chirp length of 0.4333 s. The FFT analysis consists of 512 length segments with 50% overlap, resulting in 7 overlapping segments. The resulting Doppler power spectra shown in the plot are normalized by their maximum values.

chirp creates a data point for each range bin (r); corresponding data points from the same range bin from all consecutive chirps are used to create a time series R_k (i = 1, M), where M is the number of chirps and k denotes a particular range bin (r_k). As an example, for range r_k a time series is created:

$$R_k(i) = [G_1(r_k), \ldots, G_{i-1}(r_k),\ G_i(r_k), G_{i+1}(r_k), \ldots, G_M(r_k)], \tag{2}$$

where i (=1, M) is the chirp number. The time interval between data points is the chirp duration (T).

Subsequently, each range sorted time series (i.e., a series per range bin k) is subjected to a second FFT:

$$P_k(f_D) = \mathrm{FFT}[R_k(i)], \tag{3}$$

which produces an amplitude $|P_k|$ and phase $\tan^{-1}[\mathrm{Re}(P_k)/\mathrm{Im}(P_k)]$ for each Doppler frequency (f_D). The amplitudes squared ($|P_k|^2$) constitute the familiar Doppler power spectrum for a single range bin, shown as the blue line in Fig. 1.

In the following sections, the description of the methods for surface current analysis pertains to the Doppler spectrum (amplitude and phase) from a single range bin; the same methodology is applied to each one of the range bins separately.

b. Beamforming

Each antenna receives backscattered signals from many directions at once; therefore, the energy of the single antenna Doppler spectrum (blue line in Fig. 1) contains information originating from multiple directions. Beamforming combines the amplitudes and phases from all receive antennas and effectively "points" the receiving array's sensitivity to a particular direction of interest by suppressing backscattered signals from other directions (red line in Fig. 1). For a linear array, beamforming perpendicular to the array (along the radar boresight, θ_b) to a surface patch of the ocean at range r_k, very far away ($L_N \ll r_k$, where L_N is the length of the linear array) is performed by adding the individual antenna Fourier coefficients [obtained from (3)] together,

$$B(f_D, r_k, \theta_b) \approx \sum_{j=1}^{N} P_k^j(f), \tag{4}$$

where j (=1 to N) is the antenna number of the N element receiving array.

To "steer" the beam to a particular direction, a phase shift is first subtracted from the signal from each antenna to compensate for the difference in time of arrival. A backscattered signal from range bin k (measured from the center of the receiving array) at an angle θ measured counterclockwise from east (polar coordinates) will result in a phase $\phi_k^j(\theta)$ in the received signal at each antenna j. Assuming a planar approximation of Earth this phase can be estimated as

$$\phi_k^j(\theta) = 2\pi\lambda_R^{-1}[(r_k\cos\theta - x_j)^2 + (r_k\sin\theta - y_j)^2]^{1/2}, \tag{5}$$

where x_j (easting) and y_j (northing) are the antenna positions measured from the center of the receiving array and λ_R is the wavelength of the radio wave transmitted by the HF radar. Beamforming to this location is performed by subtracting the theoretical phase shift $\phi_k^j(\theta)$ from each complex Fourier coefficient P_k^j, for each antenna j. Then these values from all N receiving antennas are summed so that

$$B(f_D, r_k, \theta) = \sum_{j=1}^{N} w_j P_k^j(f_D) e^{-i\phi_k^j(\theta)}. \tag{6}$$

An example of the power, $|B|^2$, of the beamformed signal for a single range cell (r_{20}) and beam direction (0°), which is

along the boresight ($\theta - \theta_b = 0°$), is shown in Fig. 1 (red line). Usually, a Hamming or an ultraspherical window (w_j) is applied before beamforming (see Gurgel et al. 1999b; Helzel and Kniephoff 2010) to increase suppression of unwanted signals coming from directions other than the beam direction (sidelobe effects), usually at the cost of a wider beam. General practice is to use Hamming for 8–12-antenna and ultraspherical for 12–16-antenna BLA systems (see Helzel and Kniephoff 2010).

The derived Doppler spectrum is then used to identify the Bragg peaks and measure their frequency shift (Δ_f) from the theoretical (still-water) value, which is then used to estimate the radial current ($u = \Delta f \lambda_B$, where λ_B is the Bragg wavelength) along that direction (Gurgel et al. 1999a). This process is repeated for all Doppler spectra from all ranges and directions of interest. It should be noted that for beamformed Doppler spectra the Bragg peaks are relatively narrow, and any broadening is attributed mainly to diversity in current velocities within the patch of the ocean the Doppler spectrum corresponds to (i.e., current shear, etc.; Zhang et al. 2012).

c. *Direction finding*

While beamforming "steers" the radar toward a particular location and then analyzes the beamformed signal to estimate the corresponding Doppler spectrum from that location [$B(f_D, r_k, \theta)$, see (6)], DF performs the inverse operation; it starts with the signals in each antenna and calculates the most likely direction(s) the signals originated from (e.g., Read 1989). The received signals are due to Bragg scattering from Bragg waves and the direction(s) these signals were scattered from are defined as the DOAs. DF uses the complex Doppler spectra $P_k^j(f_D)$ from all antennas (Barrick and Lipa 1997) to calculate single or multiple DOAs for each frequency bin f (Barrick and Lipa 1999):

$$\theta_{\mathrm{DOA}}(r_k, f_D) = \mathrm{DF}[P_k^{j=1,N}(f_D)], \tag{7}$$

where $P_k^j(f_D)$ are the Fourier coefficients corresponding to antenna j for a given range (r_k) and Doppler frequency bin (f_D).

For each range bin and each antenna, the Doppler spectrum [$P_k^j(f_D)$, see (3)] has distinctive Bragg peaks (see the two large peaks near the still-water Bragg peaks from individual antenna, blue line in Fig. 1). In contrast to beamforming (red line in Fig. 1) the Bragg peaks from individual antennas are broader and span multiple frequencies; each frequency within the broad peaks corresponds to a different offset from the still-water Bragg peak location. These different frequency offsets represent different values of ocean currents corresponding to different patches of the ocean of the same range but with different azimuthal angles. Although DF algorithms can be used on all the frequencies in the Doppler spectra $P_k^j(f_D)$, in surface ocean current estimation only the frequencies that lie within a range of the theoretical Bragg peak are considered. This frequency range (Bragg region) is often defined by the SNR level (e.g., Lipa et al. 2006) and its correspondence to within certain current velocity limits (e.g., ± 1 m s^{-1} from the still-water Bragg peak location). Other more advanced Bragg region selection techniques have been developed (e.g., Kirincich et al. 2019) that are not reviewed here as this is beyond the scope of the paper.

In comparing beamforming and direction finding, certain differences should be noted. In practice beamformed Doppler spectra are limited by beamwidth and steering angle resolution, which are functions of the antenna array geometry (i.e., a longer array with more antennas can provide a narrower beam and higher steering resolution). However, this is not the case for DF methods, as they are able to obtain a number of solutions, which is proportional to the number of frequency bins that lie within the Bragg region and also the number of RX antennas (Sentchev et al. 2013). Usually, this results in numerous gaps in the radar coverage area (Liu et al. 2014), which in practice can be filled in using interpolation techniques.

Although several DF algorithms have been developed (see Tuncer and Friedlander 2009) MUSIC is the most popular, primarily because of its computational efficiency. MUSIC is routinely used to analyze the signal from the commercially available CCL radar systems (i.e., CODARs Ocean Sensors) that use a single monopole antenna and two orthogonal loop antennas (Barrick et al. 1994). More recently, the maximum likelihood method has shown some promise in improving surface currents estimates with CCL systems (Emery 2020); however, to our knowledge this method is not used operationally yet. Beamscan is a DF algorithm based on beamforming and therefore is applicable to beamforming systems. Due to the ease of implementation only Beamscan and MUSIC (the most common and popular DF method in HF radars) are considered in this study and briefly described below.

1) BEAMSCAN DF METHOD

The Beamscan algorithm can only be utilized by beamforming systems (Tuncer and Friedlander 2009) and it is not a subspace method. Although it can use an array covariance matrix created from several samples (e.g., Krim and Viberg 1996), in this application we use (6), which requires the estimation of a single complex Fourier coefficient P_{k,f_D}^j for each antenna. The latter corresponds to a single frequency of the complex Doppler spectra [$P_k^j(f_D)$, see (3)]. The DOAs of this frequency (f_D) are determined by beamforming P_{k,f_D}^j [using (6)]. This creates a Beamscan spatial spectrum $B_{r_k,f_D}(\theta)$ for the particular Doppler frequency (i.e., f_D is fixed) as a function of θ (see Fig. 2). The DOA(s) corresponding to f_D are determined by the peak(s) found in the Beamscan spatial spectrum. Although Beamscan can detect DOAs from multiple directions, noise and sidelobe interference can overwhelm weaker signals resulting in false or inaccurate DOA solutions. This is shown in Fig. 2 where synthetic spectra corresponding to one (Fig. 2a) and four (Fig. 2b) DOAs are shown. Additionally, accurate identification of the DOAs requires they are separated by more than the beamwidth of the radar array. This is shown in Fig. 2b where the signals from 0° and 10° are spaced apart by an angle that is smaller than the system's beamwidth (15°); this results in incorrect Beamscan DOA estimates 15°of −5° and 13°. To reduce the number of inaccurate solutions, in this study only the DOA solution corresponding to the largest peak is used with the Beamscan method.

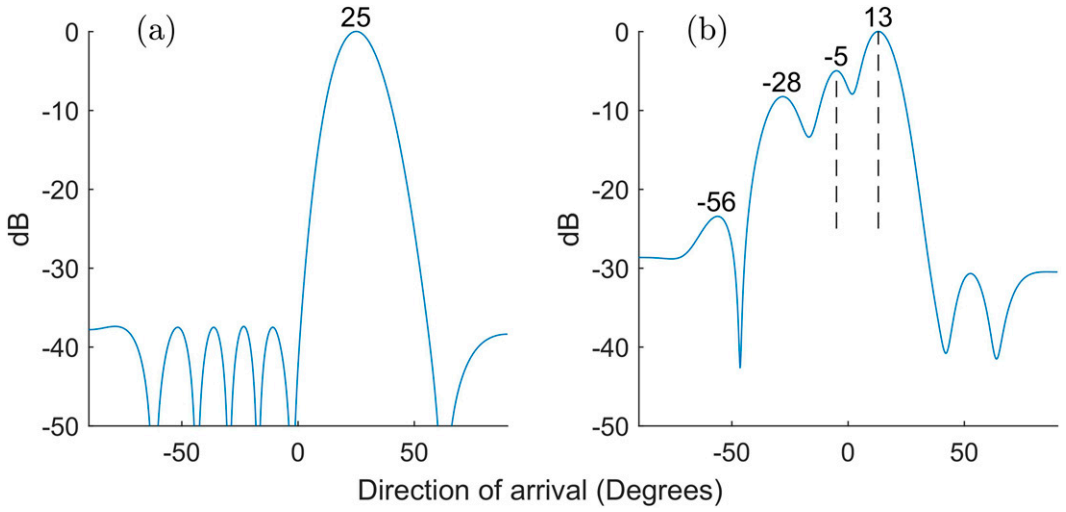

FIG. 2. Examples of idealized (no noise) synthetic Beamscan spectra: (a) single DOA with the signal arriving from 25° off the boresight and with 0 dB amplitude. (b) Four DOAs arriving from −45°, −30°, 0°, and 10° with amplitudes of −20, −10, −3, and 0 dB, respectively. The numbers on the plots correspond to the DOA angles as identified by the peaks in the Beamscan spectrum.

Beamforming and Beamscan derived Doppler spectra are shown in Fig. 3 where a simplistic model of the Doppler spectrum over azimuth [see (6) where θ is on the x axis and f_D is on the y axis] for a single Bragg peak, that has been Doppler shifted by a current parallel to shore (and where the frequency of the Bragg wave has been shifted to 0 Hz) is shown.

Analyzing each direction separately (giving plots of power versus frequency) is the beamforming method commercial HF radars use (see Fig. 3b, which corresponds to the frequency slice of the white arrow marked beamforming in Fig. 3a). The current is determined from the frequency shift of the SNR weighted location of the Bragg peak, marked as a black circle in Fig. 3b. The direction finding version of beamforming (Beamscan), analyzes each frequency separately (giving plots of power versus direction of arrival) as shown in Fig. 3c (which corresponds to the direction of boresight slice of the white arrow marked Beamscan in Fig. 3a) where a single Beamscan spatial spectrum at −0.05 Hz is presented. The current is determined by −0.05 Hz and the location of this current is defined by the location of the peak of the Beamscan spatial spectrum in Fig. 3c, marked as the red square.

The estimated currents from beamforming and Beamscan are plotted in Fig. 3a (as black circles and red squares, respectively), where the direction of the current is on the x axis and the frequency shift of the current is on the y axis. These current estimates show that these two methods produce different results.

2) MUSIC DF METHOD

The application of MUSIC involves processing each frequency separately, similarly to the application of Beamscan as explained earlier. However, MUSIC, being a subspace method, requires multiple samples of the signal in each frequency bin (Schmidt 1986), while Beamscan can be implemented using a single sample in each frequency bin, although multiple samples can also be used (e.g., Krim and Viberg 1996). Therefore, for each antenna multiple complex Fourier coefficients P^j_{k,f_D} are required; these are created by splitting a single long radar acquisition into multiple subsamples so that multiple complex Doppler spectra [$P^j_k(f_D)$, see (3)] are created for each antenna (see Barrick and Lipa 1997). This requires longer transmission times and in practice results in radial velocity estimates at intervals of 30 min or longer, depending on environmental conditions and noise (Gurgel et al. 1999b). Detailed description of the use of MUSIC for HF radar compact antenna systems is given in Barrick and Lipa (1997).

Following Barrick and Lipa (1997), each radar acquisition or subsample (called a "sample" from now on) provides a Doppler spectrum $P^j_k(f_D)$ estimate for each antenna j. For a single frequency and each antenna j, a vector of the complex Fourier coefficients P^j_{k,f_D} is created, $\mathbf{X} = [P^j_{k,f_D}]$. Subsequently, an $N \times N$ signal matrix $\mathbf{S}$ is formed by multiplying this vector by its conjugate transpose, $\mathbf{S} = \mathbf{X}\mathbf{X}^{\mathrm{H}}$. Several signal matrices $\mathbf{S}$ are created from a number (M) of consecutive radar acquisitions with each acquisition providing a P^j_{k,f_D} value. The receive matrices $\mathbf{S}$ are averaged to produce a covariance matrix, $\mathbf{C}$, so that

$$\mathbf{C} = \frac{1}{M}\sum_{i=1}^{M} \mathbf{X}(i)\mathbf{X}^{\mathrm{H}}(i). \tag{8}$$

The maximum number of DOAs (D) that can be calculated using the MUSIC algorithm is constrained by the number of acquisitions used for averaging (M) and the number of antennas (N), so that D must satisfy both conditions $D \leq M$ and $D \leq N - 1$.

The eigenvalues and eigenvectors of the covariance matrix $\mathbf{C}$ represent the signal(s) and noise for the particular frequency (see Fig. 4a). The largest eigenvalues and corresponding eigenvectors

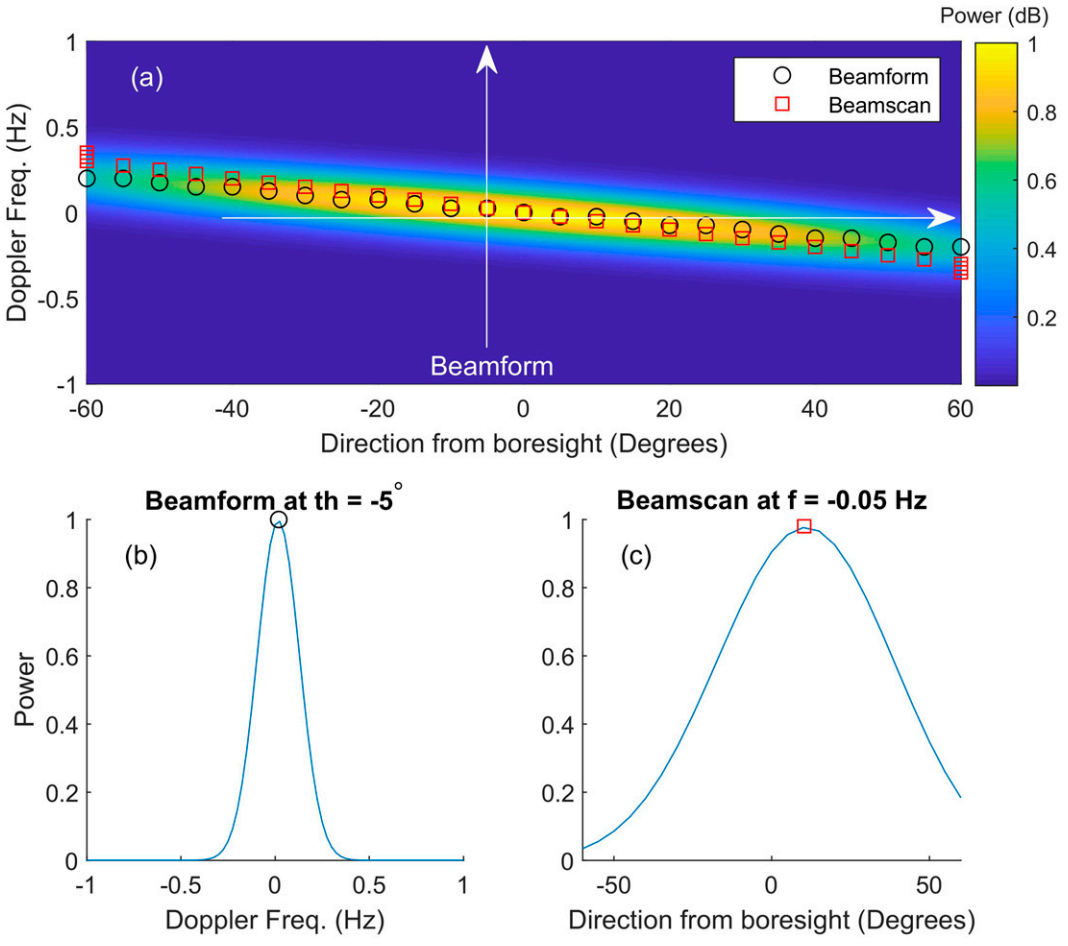

FIG. 3. (a) Beamformed Doppler spatial spectrum; Doppler frequency spectra as function of direction from boresight created by modeling a current parallel to shore for the incoming Bragg peak (see section 4f), where its still-water location has been shifted to 0 Hz. White arrows correspond to the frequency (−0.05 Hz) and direction from boresight (−5°) slices for (b) beamforming and (c) Beamscan.

represent the DOAs while the remaining eigenvalues represent noise. A noise matrix is created, where the $N - D$ noise eigenvectors form the columns of the noise matrix $\mathbf{E}_n = [\mathbf{E}_n]$, an $N \times N - D$ matrix. The MUSIC pseudospectrum $P_{\mathrm{MU}}(\theta)$ is defined as

$$P_{\mathrm{MU}}(\theta) = \frac{1}{\mathbf{A}^{\mathrm{H}}(\theta)\mathbf{E}_n\mathbf{E}_n^{\mathrm{H}}\mathbf{A}(\theta)}, \tag{9}$$

where $\mathbf{A}(\theta) = [a_j(\theta)]$ is a column vector of the complex antenna patterns $a_j(\theta)$. The D largest maxima in $P_{\mathrm{MU}}(\theta)$ correspond to the D direction of arrival(s) of the signal(s) within this frequency bin. More details can be found in Barrick and Lipa (1999), who provided a thorough description of the application of MUSIC to CCL HF radar systems.

The process in choosing how many sources ($D = 1$ to $N - 1$) are present in a particular frequency bin is key to acquiring accurate DOAs and several different methods have been employed (e.g., Barrick and Lipa 1997; Laws et al. 2000). The approach used here is called MUSIC-highest and it has been described in detail in Kirincich et al. (2019). The method assesses the DOA function $P_{\mathrm{MU}}(\theta)$ for each different number of signals (1 to $N - 1$) and then the highest number of DOAs (D) where the MUSIC pseudospectrum $P_{\mathrm{MU}}(\theta)$ has the same number of peaks as the number of DOAs (D) is chosen.

An example of this analysis is presented in Fig. 4 using synthetic data. Two uncorrelated signals were created with DOAs of 15° and 25° and corresponding signal amplitudes of −10 and 0 dB, respectively. Then a −10 dB of Gaussian noise was added to them. Using this synthetic signal, a covariance matrix was created with 20 samples assuming a 12-antenna linear array with 0.45λ antenna spacing. The sorted eigenvalues from the eigen decomposition of the covariance matrix are shown in Fig. 4a. The corresponding MUSIC DOA pseudospectrum $P_{\mathrm{MU}}(\theta)$ for $D = 2$ (2 DOAs) is shown in Fig. 4b. Pseudospectra for $D = 1$–11 DOAs are shown in Fig. 4c. It is worth noting that some of the pseudospectra in Fig. 4c show an incorrect number of DOAs; i.e., $D \neq 2$ with additional peaks at locations other than the prescribed 15° and 25°. For example, the top magenta line in Fig. 4c shows the MUSIC

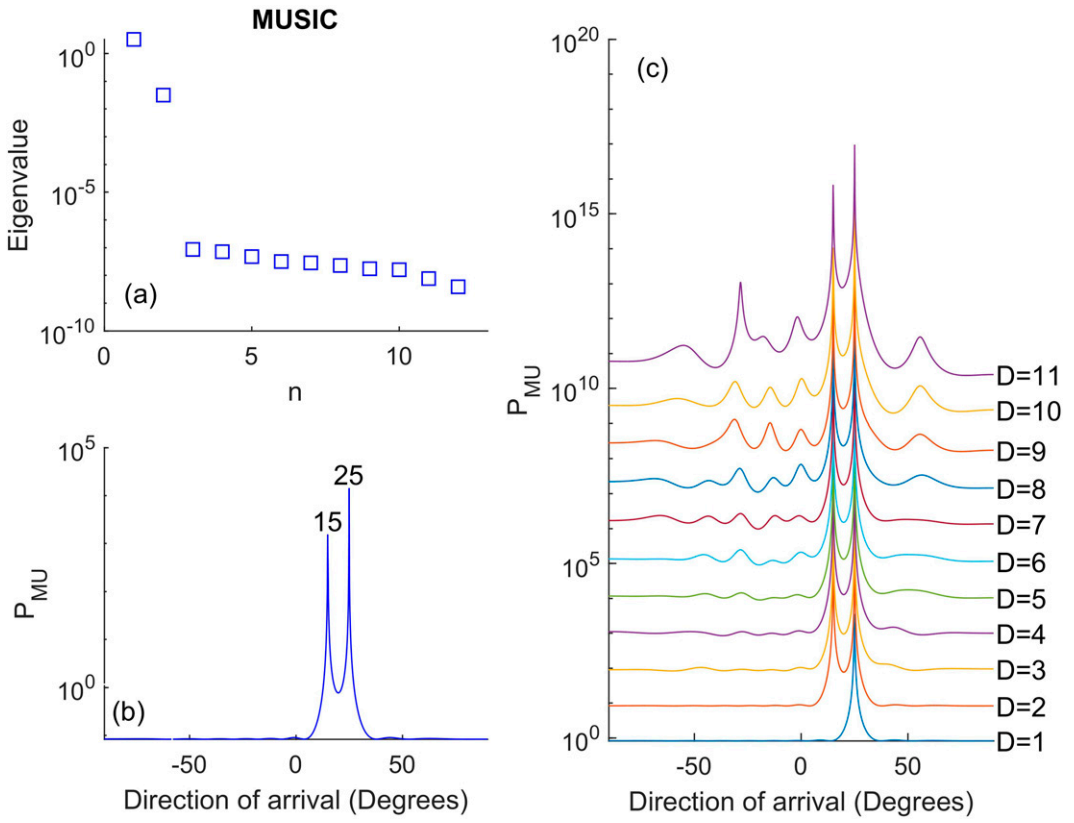

FIG. 4. Example of MUSIC analysis using a synthetic covariance matrix created with 20 samples assuming a 12-antenna linear array with 0.45λ antenna spacing. The input consists of two uncorrelated signals with DOAs at 15° and 25°, signal amplitudes of −10 and 0 dB, respectively, and −10 dB Gaussian noise. (a) Eigenvalue decomposition of the covariance matrix; (b) corresponding MUSIC pseudospectrum for the 2 DOA solution; (c) the 11 MUSIC pseudospectra (artificially vertically offset for clarity) corresponding to the 1–11 DOA solutions.

pseudospectrum for $D = 11$ and contains 5 prominent peaks, although there are only two actual DOAs. Only the $D = 2$ pseudospectrum contains the same number of peaks as D, and therefore, $D = 2$ corresponds to MUSIC-highest, which gives the correct solution.

3. Data availability and processing

For this study, two HF radars are used to estimate surface ocean currents at three sites in Long Bay, off the South Carolina (United States) coastline (see Fig. 5). Long Bay extends some 100 km along the coast and shelf circulation is predominantly influenced by local winds and the passage of low pressure synoptic fronts (Wu et al. 2017). Despite the local extent of the synoptic fronts, their predominant directions (from NE or SW) result in highly energetic wave events with high oblique angles of approach near the coastline (Voulgaris et al. 2008). On average, wind speed is stronger offshore and reduced inshore (Wu et al. 2018); therefore, offshore wave heights are expected to be larger than inshore wave heights. In situ measurements (Gutierrez 2006) have shown that tidal oscillations account for 30%–45% of the total current variability. In the inner-shelf M_2 alongshore-current amplitudes increase with proximity to the coastline where they dominate over cross-shore tidal flows. Further offshore, the cross-shore current tidal amplitudes decrease seaward in agreement with Poincaré wave theory.

a. Comparison sites and in situ data

The location of the sites with in situ current data available are shown in Fig. 5. They are denoted as ADCP1 and SSBN7 and are located at (33.379°N, 78.347°W) and (33.841°N, 78.482°W) corresponding to water depths of 25 and 10 m, respectively. Data from site ADCP1 were collected using a bottom mounted 600 kHz ADCP configured to collect data with a vertical resolution of 1 m; the topmost usable bin was located 3.1 m below the surface. Currents were recorded every 20 min and each record was the average of a 14 min ensemble. Data for site SSBN7 were obtained from NOAA/NDBC (https://www.ndbc.noaa.gov/station_page.php?station=ssbn7) that stores current data collected by a bottom mounted 600 kHz ADCP deployed at 10 m water depth and operated by the Coastal Ocean Research and Monitoring Program (CORMP; Bushnell et al. 2018).The system was configured to collect data representing ensemble averages of 10 min, with a bin size of 1 m and the uppermost bin is centered 1 m below the surface.

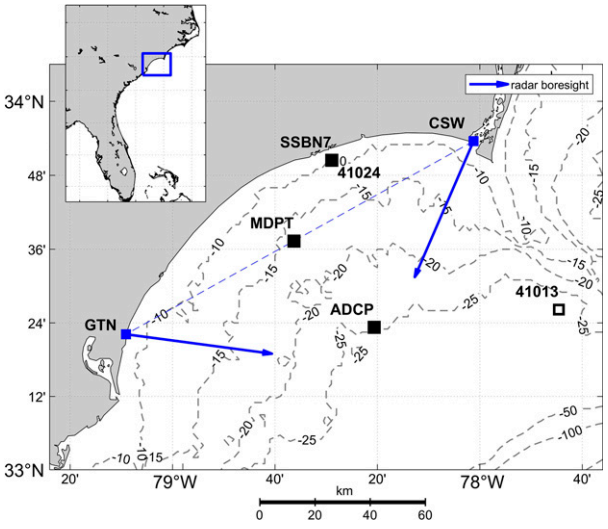

FIG. 5. Study site location showing HF radar sites (GTN and CSW, blue squares) and their boresight (or radar look) directions (blue arrows; for angle values, see Table 2). In situ current meter deployment locations (ADCP1 and SSBN7) and the baseline midpoint (MDPT) between the two radar sites are shown (black squares). Wind data were obtained from NDBC buoys 41013 and 41024 (open squares). Bathymetry contours shown in meters.

ADCP1 is located close to the radar boresights (see Fig. 5), corresponding to radar beam directions of 4.9° and 9.4° and ranges of 63.5 and 75.2 km for radar sites CSW and GTN, respectively. On the other hand, SSBN7 is near the limits of beamforming (±60°) corresponding to beam directions of −59.1° and 47.9° from the radar boresight and ranges of 43.1 and 81.3 km for CSW and GTN, respectively.

The third site selected is the midpoint (MDPT) location (33.622°N, 78.6047°W) along the baseline between the two radars (see Fig. 5); it corresponds to beam angles of −37.1° and 38.1° for CSW and GTN, respectively and a range of 60 km (see Table 1). At this location it is expected that the two systems would provide the same radial velocity but with opposite sign.

b. *HF radar data*

The two HF radar systems used are located at Fort Caswell, North Carolina (CSW), and Georgetown, South Carolina (GTN), as shown in Fig. 5. The systems are part of the NOAA Integrated Ocean Observing Systems (IOOS). Both systems are operated by the University of South Carolina, Columbia, since February 2012, and consist of a 12 antenna linear receiving array spaced 0.45λ apart (where λ is transmit wavelength, ≈36 m). The HF systems are WERAs manufactured by Helzel Messtechnik Gmbh (see Gurgel et al. 1999a). The transmit array consists of four monopole antennas arranged in a rectangular configuration (0.5λ by 0.15λ spacing) with the rear antennas having a phase delay of 0.35λ so that radiation toward land is suppressed. Both receive and transmit arrays are constructed using resonant monopole antennas with three elevated radials; their boresights are −113.4° and −7.6° (mathematical convection, counterclockwise from east) for CSW and GTN, respectively (see Fig. 5 and Table 1). The systems operate in "listen before talk" mode, and the transmit frequency is set between 8.2 and 8.4 MHz depending on ambient noise and/or radio interference detected prior to transmitting. They transmit a frequency modulated continuous waveform (FMCW) with a 50 kHz bandwidth that results in 3 km range resolution. The Bragg waves that reflect the transmitted signal have wavelengths between 17.9 and 18.3 m depending on the exact frequency of transmission. For a nominal frequency of 8.3 MHz the Bragg peaks appears at ±0.294 Hz, assuming no mean flow and deep water conditions. Each radar acquisition consists of 2048 chirps of 0.433 33 s length each, resulting in an acquisition time of approximately 14.8 min. Acquisition is repeated every 30 min in order to reduce power consumption and allow the air conditioner to keep the electronics trailer cool in the subtropical climate. The details of the HF radar systems used are listed in Table 2.

In the radar systems used in this study, processing up to and including (2) is completed in the radio system itself before data are sent to the control PC. All further processing is carried out using MATLAB software developed by the authors utilizing the full wave dispersion solution to estimate Bragg frequency even at shallow waters. The Beamscan direction finding along with the beamforming and MUSIC MATLAB codes used here are available in Cahl and Voulgaris (2022), while codes for reading WERA raw data are available in Voulgaris and Cahl (2020).

Application of both beamforming and DF methods require a priori knowledge of the antenna pattern (i.e., phase and amplitude as a function of boresight direction) for each element

TABLE 1. HF radar beam characteristics at the comparison sites and % of successful radial current estimates (S) for each of the methods used. Radial directions are in mathematical convention, counterclockwise from east, while beam directions are with reference to the radar boresight (−113.4°and −7.6° for CSW and GTN, respectively).

					Successful estimates (S; %)		
HF radar	Site	Radial direction (°)	Beam direction (°)	Range (km)	Beamform	Beamscan	MUSIC
CSW	ADCP1	−118.3	−4.9	63.5	91	99	97
	SSBN7	−172.5	−59.1	43.1	89	54	34
	MDPT	−150.5	−37.1	60.0	84	90	74
GTN	ADCP1	1.8	9.4	75.2	78	94	93
	SSBN7	40.3	47.9	81.3	59	45	42
	MDPT	30.5	38.1	60.0	86	81	88

TABLE 2. HF radar specifications used in this study. Bragg wavelength and other quantities dependent on the operating frequency are calculated using 8.3 MHz. Note that λ_R is the radar transmit wavelength.

Variable	Value/description
Operating frequency (f_R)	8.2–8.4 MHz
Bandwidth (B)	50 kHz
Range resolution (Δr)	3 km
Number of RX antennas (N)	12
Antenna type	Monopole (three elevated radials)
Antenna spacing ($0.45\lambda_R$)	16.25 m
Chirp length (T)	0.4333 s
Chirps per acquisition (M)	2048
Bragg wavelength (λ_B)	18.1 m
Effective depth	1.4 m
Bragg wave frequency (f_B)	0.294 Hz
Transmit array	Four antennas, directed
Transmit waveform	FMCW

of the array. In this study, theoretical antenna patterns [$e^{i\phi_j}$, see (5) for ϕ_j] are used, assuming a constant amplitude (i.e., a radially symmetric monopole antenna pattern). It should be noted here that in addition to extensive tuning, MUSIC also is known to often require antenna pattern measurements for accurate ocean current measurements (Kohut and Glenn 2003), which were not available in this study.

The effective depth of the current the HF radar measures (Stewart and Joy 1974) is approximately 1.4 m (Bragg wavelength divided by 4π). This depth is close to the in situ measurements at SSBN7 (1 m) but only half the depth of the in situ measurements at ADCP1 (3.1 m). However, we still expect high correlation for a 1.7 m difference in depth at ADCP1. We do not attempt to apply any shear profile to compensate for this difference in depth as the focus of this paper is mainly a comparison between the HF radar algorithms.

1) BEAMFORMING

To reduce noise levels, Doppler spectra for beamforming HF radars are typically averages of several individual spectra from overlapping series. In this study, three different FFT analysis lengths were tested for beamforming and Beamscan: a single 2048-point FFT (0.0011 Hz Doppler resolution), three 1024-point windows (0.022 Hz) with 50% overlap, and seven 512-point (0.044 Hz) windows with 50% overlap. The results from each of these FFT analysis lengths were compared against in situ measurements corresponding to a period of a week ("test data," not shown here). It was found that for beamforming, the 512-point windows provide surface currents that agree best (R^2 and RMSD) with the in situ measurements. This window is similar to that used in the manufacturer's software and reduces the frequency resolution by a factor of 4.

Beamforming is limited to ±60° from the boresight for a 12-antenna linear array. For computational efficiency, the beamform spectrum $B_{r_k,\theta}(f_D)$ is calculated in increments of 1°, resulting in 121 beamformed spectra over the above-mentioned range. However, the beamwidth of 15° in our experimental setup suggests that the 121 spectra are not truly independent for each.

For each beamformed Doppler spectrum $B_{r_k,\theta}(f_D)$, the Bragg peaks are identified. The largest peak within the Doppler frequency range ±0.055 Hz around the theoretical Bragg frequency (f_B), which corresponds to a radial velocity range of ±1 m s^{-1} is identified. The required SNR that this peak have was set to 15 dB. This value was selected after trying a range of values (5–25 dB) and comparing the resulting surface currents to those from the "test data" (see above). If it is not above this limit, beamforming does not return a result.

Then the frequency location of this Bragg peak is determined. The accuracy of this estimate is defined by the Doppler frequency resolution (0.0044 Hz) and corresponds to a radial velocity of approximately 8 cm s^{-1}. To increase the accuracy above, defined by the resolution of the Doppler spectra, the surrounding 2 points on either side of the peak identified are used to calculate a 5-point SNR-weighted peak frequency (e.g., Wang et al. 2014),

$$f_p = \frac{\sum_{i=n-2}^{n+2} f_i[B_{r_k,\theta}(f_i) - \sigma_{\text{no}}]}{\sum_{i=n-2}^{n+2} [B_{r_k,\theta}(f_i) - \sigma_{\text{no}}]}, \tag{10}$$

where $B_{r_k,\theta}$ is the spectral energy at frequency f_i, n is the index of the frequency bin that the maximum energy is identified, and σ_{no} is the noise level of the Doppler spectrum. The latter is estimated using the method described in Hildebrand and Sekhon (1974). The radial surface current is estimated from this peak frequency, $u = (f_p - f_B)\lambda_B$, where f_B and λ_B are the theoretical Bragg frequency and wavelength, respectively.

2) DIRECTION FINDING

Application of the DF algorithm (7) requires that the Doppler frequencies within the Bragg regions are identified. This identification occurs for each range cell k using the corresponding, averaged Doppler power spectrum $\overline{P_k}(f_D)$, which is defined as

$$\overline{P_k}(f_D) = \frac{1}{N}\sum_{j=1}^{N} |P_k^j(f_D)|^2, \tag{11}$$

where j is the antenna number.

The frequency bins within $\overline{P_k}(f_D)$ where the energy is at least 5 dB above the noise level and within ±1 m s^{-1} of the still-water Bragg peak frequency (i.e., f_B ± 0.055 Hz) are identified. Higher SNR limits (10–15 dB) were assessed but this led to significant reduction to data availability; therefore, the 5 dB limit was chosen. In this study, for each frequency f_D within the Bragg region, the Beamscan algorithm calculates a single DOA, while MUSIC is limited to a maximum of 5 DOAs as using a higher or lower DOA limit resulted in decreased accuracy.

For Beamscan, the same three FFT options as for beamforming (i.e., a single 2048-point FFT, three 1024-point FFT with 50% overlap, and seven 512-point FFT with 50% overlap

segments) were considered and were compared against the "test data" (not shown here). It was found that the 2048-point FFT, using the entire 14.8 min acquisition to create Doppler spectra, $P_k^{j=1,N}(f_D)$ with a resolution of 0.0011 Hz (equivalent to surface current resolution of ≈2 cm s^{-1}) performed best.

MUSIC requires averaging several subsamples of the received signal to produce the covariance matrix **C**. The minimum number of subsamples required (M) for creating covariance matrix is the same as the number of antennas available (Tuncer and Friedlander 2009). In our analysis the 14.8 min data acquisition was split into 1024-point (7.5-min-long) subspectra (Δf = 0.022 Hz) with 92% overlap creating a total of 13 subspectra for the covariance matrix. This results in a surface current resolution (≈4 cm s^{-1}) only twice that of Beamscan, which uses the whole sample. Additionally, 512-point subspectra with 75% overlap (13 subspectra) were considered for using MUSIC, but this did not perform as well, the results of which are not shown here.

In addition, MUSIC also required tuning for the peak threshold used in MUSIC-highest (Kirincich et al. 2019). Due to the fact that the BLA with 0.45λ element spacing provides much sharper peaks in the MUSIC pseudospectrum than with more compact arrays different DOA peak threshold values were considered in the range of 0.5–8.0; the threshold value of 2.0 performed best and it was adopted for use in the analysis presented here.

c. *Surface velocity estimation*

For each method, spurious values in the HF radar surface current estimates were identified using a wild point editing method that uses a five-point median sort filter (Justusson 1981) and then removed from further analysis. Subsequently each radar derived current time series was linearly interpolated onto the in situ time series. The availability of the post-processed radar current estimates from each method (i.e., beamforming, Beamscan, and MUSIC) after wild point removal is listed in Table 1 for both radar sites and all three locations of interest.

Prior to intercomparison the in situ current measurements at locations ADCP1 and SSBN7 (see Fig. 5) are projected into the radial components corresponding to the GTN and CSW radar sites using the radial directions listed in Table 1. The radial current from CSW is multiplied by −1 so that positive values of radial currents from both radar sites denote flow toward 30.5° N (NNE).

4. Results

a. *Wave and wind conditions*

Nearshore wave and wind conditions were obtained from SSBN7 and buoy 41024 (see Fig. 5), respectively. These stations are located just a few hundred meters from each other, so the data are assumed to be collocated. Wave direction measurements at this location are only available from 1 November to 15 December 2016. Offshore, wind speed and direction were provided from buoy 41013 (see Fig. 5), which because of its location and range from the coastline it is assumed to provide wind conditions similar to those experienced at ADCP1, the station where directional wave spectra were recorded. These measurements are shown in Fig. 6 and summarized as wind roses in Fig. 7.

The wind direction is predominantly alongshore both nearshore (buoy 41024, Fig. 7b) and offshore (buoy 41013, Fig. 7a), like the climatological averages found by Wu et al. (2017). Nearshore winds are variable 0–10 m s^{-1}, often fluctuating near the 5.3 m s^{-1} minimum wind speed required for the generation of 18.1 m (0.294 Hz) Bragg waves (see Fig. 6a) corresponding to the 8.3 MHz radar operating frequency (Shen et al. 2012). Offshore winds are stronger, in the range of 5–15 m s^{-1}, mostly above the 5.3 m s^{-1} Bragg minimum.

Wave directions offshore (ADCP1, Fig. 7c) are variable, where waves come from between east and south, with a slight preference to the southeast. Most of the time, offshore wave height is <1 m; however, there are periods where higher wave heights are observed (Fig. 6c). The wave frequency spectrum (Fig. 6e) at this location shows wind driven seas with a smooth high-frequency tail measurable above the Bragg frequency (0.294 Hz), indicated by a white line.

In the nearshore (SSBN7, Fig. 7d), when wave direction measurements were available (red line in Fig. 6d), waves are mainly from the south-southeast, perpendicular to the local coastline at this location. During July, nearshore wave heights are slightly larger than those recorded at ADCP1, while in October and thereafter nearshore wave heights are <1 m and smaller than those recorded offshore (ADCP1). Measurements of the high-frequency Bragg waves were not available at SSBN7.

b. *Doppler spectra estimates*

Doppler spectra for each antenna for the range cell and beam direction corresponding to the ADCP1 location are shown in Figs. 8 and 9 for GTN and CSW, respectively. Only a limited range of Doppler spectrum frequencies around the still-water Bragg frequency is shown for clarity. The Bragg peaks are clearly visible in the spectra for both positive (waves coming toward the radar site) and negative (waves going away from the radar site) Doppler frequencies. It is noticeable that for GTN antennas 5 and 7 had low SNR in October and November. For CSW, antennas 3 and 8 had almost no signal and were effectively not operational during the periods, 1 July–15 October, and 15 October–31 January, respectively.

The antenna malfunctions noted above suggest that beamforming for CSW may be less effective than theoretically predicted for a 12-antenna linear array. For GTN, the lower SNR in antennas 5 and 7 during October and November may result in lower beamforming performance during those times. However, the same signal is used in all methods (beamforming, Beamscan, and MUSIC) utilized in this analysis and this should not affect the intercomparison of the methods, although MUSIC is known to be sensitive to these antenna issues unless antenna grouping is used (Dumas and Guérin 2020). Furthermore, these are realistic situations representing common issues in operational oceanography, especially for

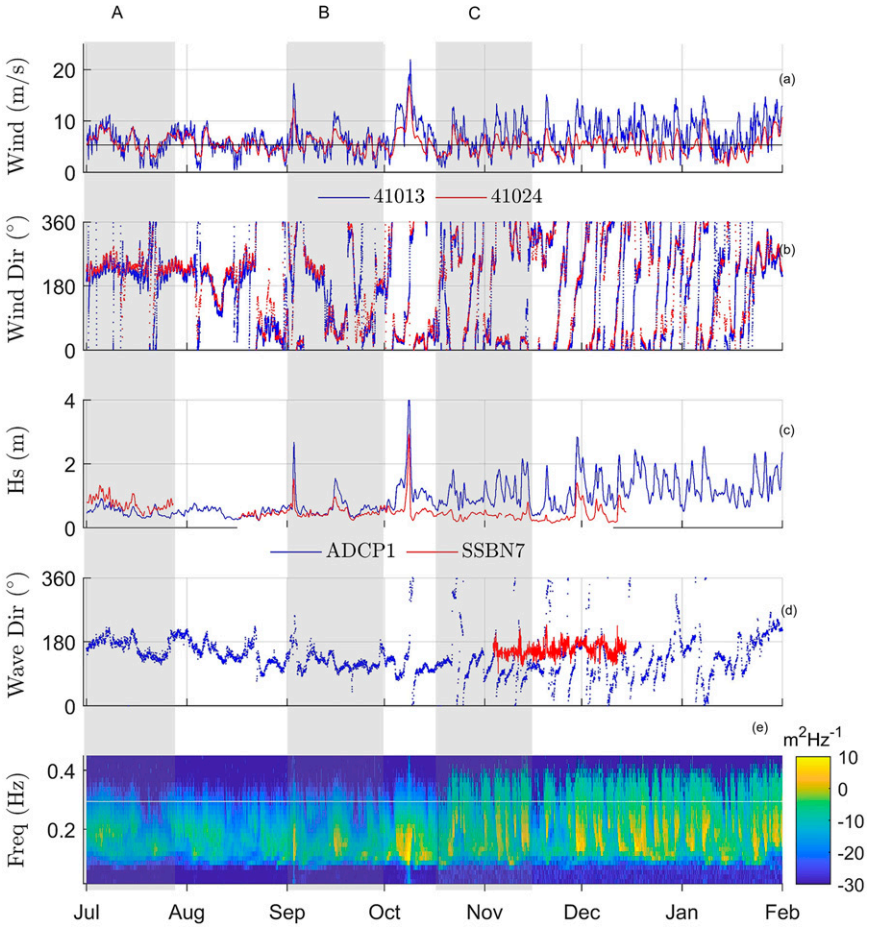

FIG. 6. Time series of (a) wind speed measured offshore (NDBC buoy 41013, blue line) and nearshore (NDBC buoy 41024, red line). The theoretical minimum wind speed required to locally generate Bragg waves for the 8.3 MHz radar sites is shown as black line. (b) Offshore (blue) and nearshore (red) wind direction. (c) Significant wave height measured at sites ADCP1 (blue) and SSBN7 (red). (d) Wave direction for ADCP1 and SSBN7 as in (c). (e) Time stack of wave energy frequency spectra for site ADCP1 (white line indicates frequency of Bragg ocean waves for an 8.3 MHz HF radar).

HF radar sites subjected to storm, coastal erosion, and/or cable damage that results in performance deterioration.

c. *Radial current estimates*

There is a significant amount of literature on optimizing MUSIC, specifically for HF radar current estimates with compact antenna systems (e.g., Barrick and Lipa 1999; Kirincich et al. 2019). Recent research has shown grouping antenna elements together into groups and averaging across these groups can be combined with self-calibration (as opposed to antenna pattern measurements) to increase the accuracy of MUSIC further (Dumas and Guérin 2020; Guérin et al. 2021). However, specific grouping and tuning parameters are site specific (Lorente et al. 2022). This is not considered within this paper, as the main focus is to compare easily implemented direction finding algorithms for a BLA radar system.

Radial current estimates from CSW and GTN using the three methods (beamforming, Beamscan, and MUSIC) were made for all three locations (ADCP1, SSBN7, and MDPT) and these are compared against the in situ data for ADCP1 and SSBN7 and between the two radar sites at MDPT. The results are shown as scatterplots in Fig. 10, and as a Taylor diagram in Fig. 11. Statistical analysis of the comparisons included estimations of correlation (R^2), regression (slope, s), bias, root-mean-square difference (RMSD) and RMSD normalized by the standard deviation of the in situ velocities (NRMSD) and the results are listed in Table 3. We note here that the p values for the R^2 and slopes are all very close to zero except for radar CSW at SSBN7 using beamforming, where the R^2 is zero and the p value is 0.04. The Taylor diagram (Fig. 11) allows the comparative assessment of the different methods using the correlation coefficient, NRMSD, and the standard deviation, the closer the results lie to the in situ measurements the better they agree (Taylor 2001). Figure 11

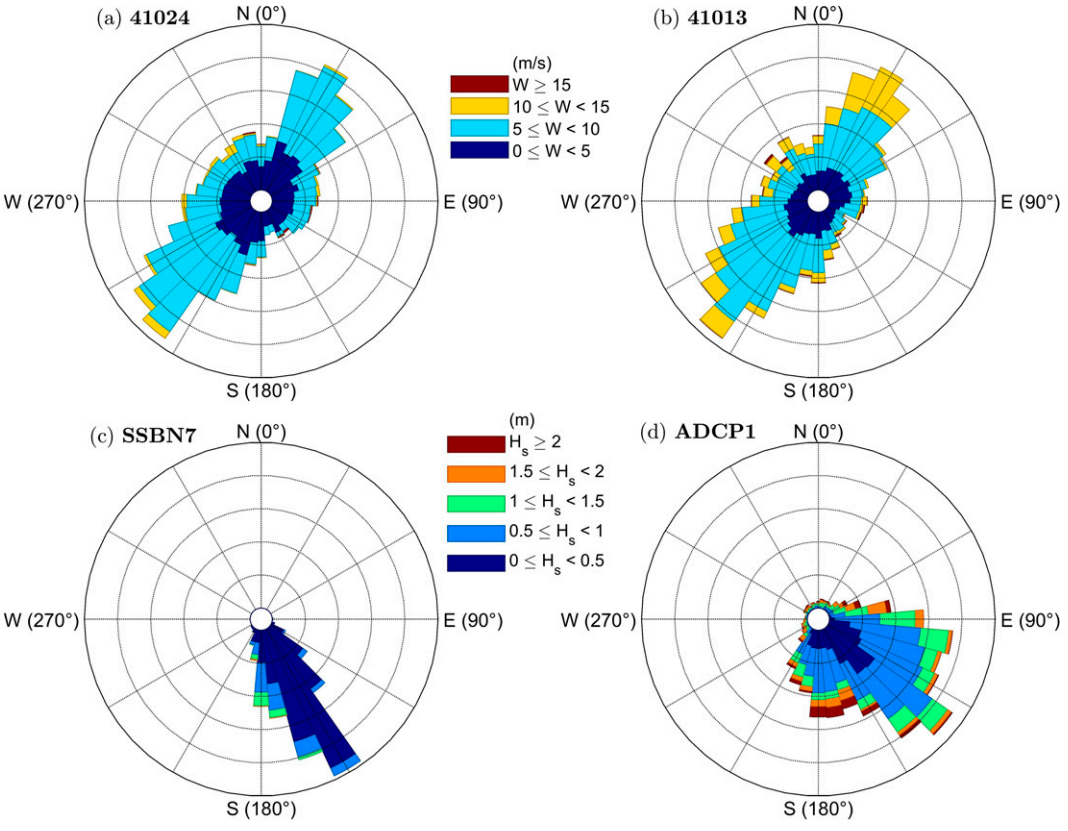

FIG. 7. Synoptic wind and wave conditions for the period of study shown as rose diagrams. Wind conditions at (a) NDBC buoy 41013 (offshore) and (b) buoy 41024 (nearshore, near site SSBN7). Wave height and peak wave energy direction for sites (c) ADCP1 and (d) SSBN7 are shown.

suggests that all methods perform similarly at ADCP1. However, at SSBN7 and MDPT, beamforming (circles) performs worse than MUSIC (squares) and Beamscan (triangles). This is described in more detail below.

1) BEAMFORMING

At location ADCP1, beamforming derived HF radar surface currents (Figs. 10a,d) correlate well with the in situ currents with $R^2 = 0.79$ for both CSW and GTN. The scatter is low with RMSD of 7.0 and 8.5 cm s^{-1} and NRMSD of 0.5 and 0.57 for CSW and GTN, respectively (see more statistics in Table 3).

For SSBN7 and MDPT locations, corresponding to higher steering angles from the radar boresight than ADCP1 (Table 1), beamforming radial current estimates do not compare as favorably with the in situ currents (see Figs. 10g,j,m). The disagreement is more pronounced for the estimates from CSW at SSBN7 where no correlation is found ($R^2 = 0$) while for GTN the correlation is still low ($R^2 = 0.29$). Similarly, no correlation ($R^2 = 0.01$) is found at MDPT. The RMSD value at location SSBN7 is almost double than that at location ADCP1 with values of 16 and 14 cm s^{-1}, and NRMSD is almost triple with values of 1.32 and 1.64 for CSW and GTN, respectively (see Table 3). At MDPT, the RMSD between the radar sites is similar (14 cm s^{-1}) to the RMSD between the radars and in situ measurements at SSBN7.

2) BEAMSCAN

Radial estimates using the Beamscan method show a reasonable correlation with the in situ radials at ADCP1 ($R^2 = 0.8$ and 0.85 for CSW and GTN, respectively; see Figs. 10b,e). It is worth noting that at this location the steering angles (−4.9° and 9.4° for CSW and GTN, respectively) are small. The regression lines have slopes slightly above 1, (1.1 for both CSW and GTN) and the bias is 0.1 cm s^{-1} for GTN and −1.2 cm s^{-1} for CSW (see Table 3). The percentage of time the method provided a solution (S) is 99% and 94% while the RMSD is 7.7 and 7.1 cm s^{-1} and NRMSD is 0.55 and 0.48 for CSW and GTN, respectively.

At SSBN7 Beamscan radial current estimates show more scatter than at MDPT (see Figs. 10h,k,n). At SSBN7, the correlation for CSW ($R^2 = 0.52$) is higher than for GTN ($R^2 = 0.32$) while at MDPT, the radars correlate well with each other ($R^2 = 0.76$). The value of S is higher for CSW (54%) than GTN (45%) at SSBN7 while at MDPT solutions were obtained for 90% and 81% of the time for CSW and GTN, respectively (see Table 1). At SSBN7, the RMSD is up to 50% higher than at location ADCP1 with values of 9.3 and 13 cm s^{-1} and NRMSD of 0.94

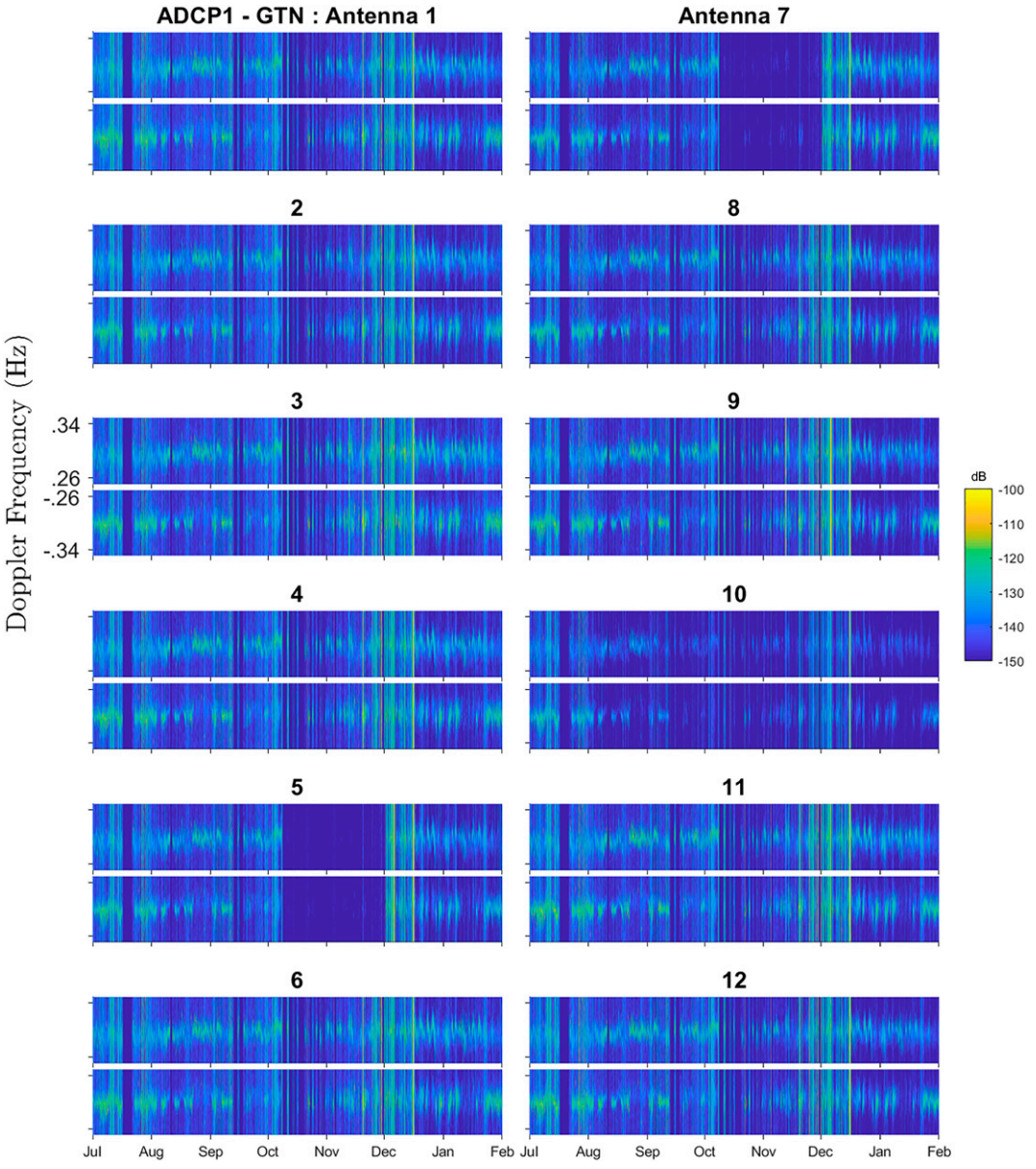

FIG. 8. Doppler spectra for GTN antennas 1–12 for the range cell corresponding to the location of ADCP1.

and 1.64 for CSW and GTN, respectively (see Table 3), while at MDPT location the RMSD (6.4 cm s^{-1}) is similar to that found for location ADCP1.

3) MUSIC

MUSIC HF radar surface current estimates at location ADCP1 show similar correlation (R^2 = 0.78 and 0.84 for radar sites CSW and GTN, respectively) than beamforming and Beamscan (Figs. 10c,f). The slope is close to 1 for both radar systems (0.92 and 1.04 for CSW and GTN, respectively) and no significant bias in the estimates is found (Table 3). The method provided solutions for 97% and 93% of the time for CSW and GTN, respectively; the RMSD is 8.1 and 7.2 cm s^{-1} and NRMSD of 0.58 and 0.48 for CSW and GTN, respectively.

At the nearshore location SSBN7 (Figs. 10i,l), higher correlation is found for CSW (R^2 = 0.42), than GTN (R^2 = 0.27). At MDPT, the radar current estimates have low correlation with each other as indicated by R^2 = 0.37 (Fig. 10o). At SSBN7, MUSIC provided solutions for 34% and 42% of the time, for CSW and GTN, respectively; these percentages are much lower than those found at location ADCP1. For MUSIC, there is better solution recovery at MDPT location (74% and 88%, for CSW and GTN, respectively—see Table 1). At SSBN7, the RMSD is 9.9 and 13 cm s^{-1} with NRMSD values of 1.1 and 1.7 for CSW and GTN,

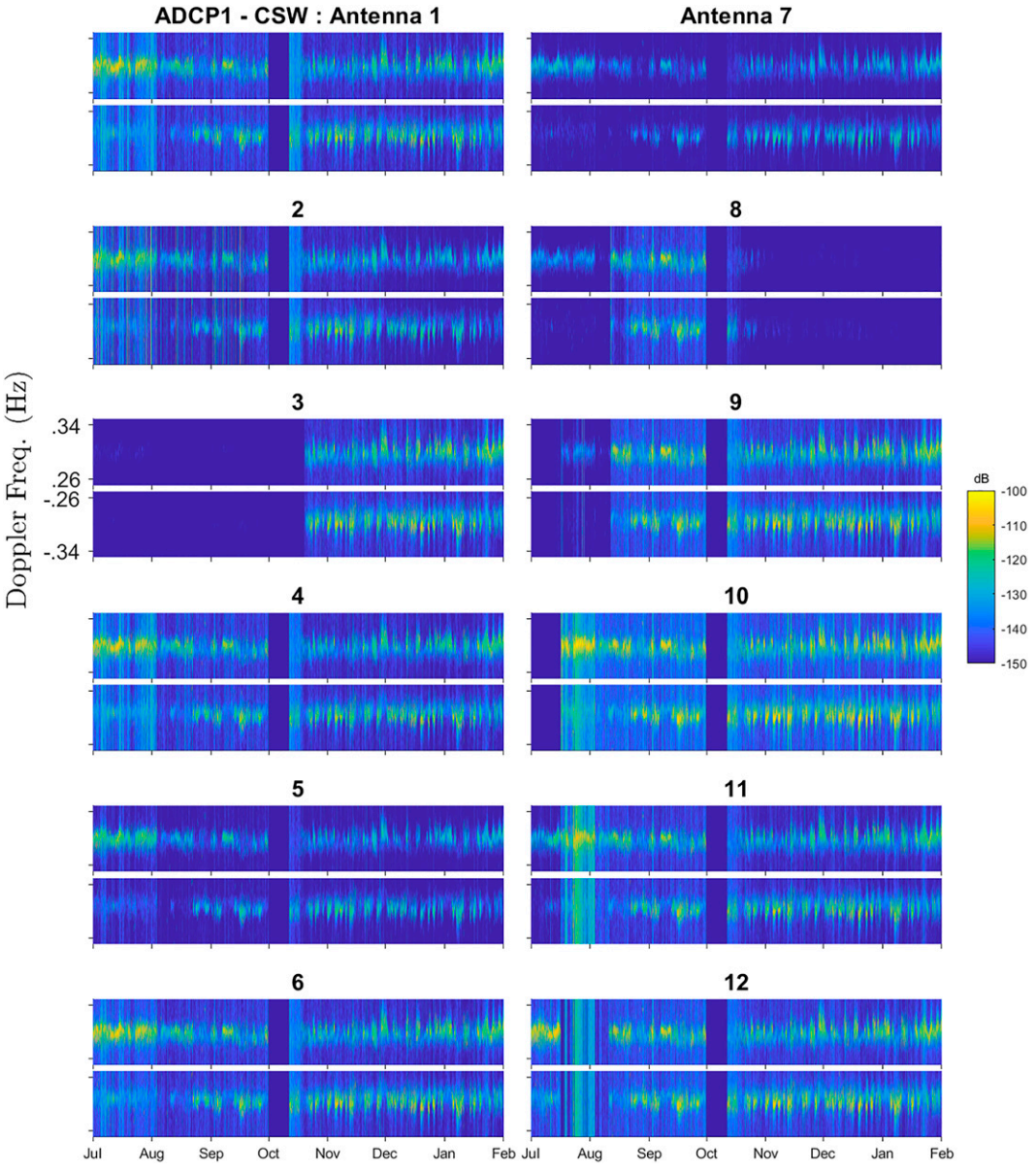

FIG. 9. Doppler spectra for CSW antennas 1–12 for the range cell corresponding to the location of ADCP1.

respectively (Table 3); an RMSD value of 10 cm s^{-1} is found at MDPT.

d. *Effect of wind and wave conditions*

To assess the accuracy of the different methods under different wind and wave conditions, representative events denoted as A, B, and C (see Fig. 6) are selected for further examination. During event A (1–27 July 2016), nearshore wave height at SSBN7 is higher than that at ADCP1 (Fig. 6c) although the wind speeds (Fig. 6a) are variable (0–10 m s^{-1}) their magnitude is similar at both nearshore and offshore locations. Wave heights are similar at both locations for event B (1–30 September 2016), although the winds near ADCP1 are slightly higher than those at SSBN7. During event C (15 October–15 November 2016), ADCP1 is experiencing significantly larger wave heights and winds than SSBN7. For site GTN, all antennas perform well (high SNR) during events A and B but have low SNR in both antennas 5 and 7 during event C. At site CSW, antenna 3 has low SNR during events A and B while antenna 8 has low SNR during event C.

For each event, as before, radial current estimates from CSW and GTN are compared to the in situ data and the estimates between the two radar sites at MDPT. Taylor diagrams in Fig. 12 summarize the accuracy of the different HF radar methods during each event at each location (ADCP1, SSBN7, and MDPT). For all events, the HF radar velocities correlate well with the in situ measurements at ADCP1 independently

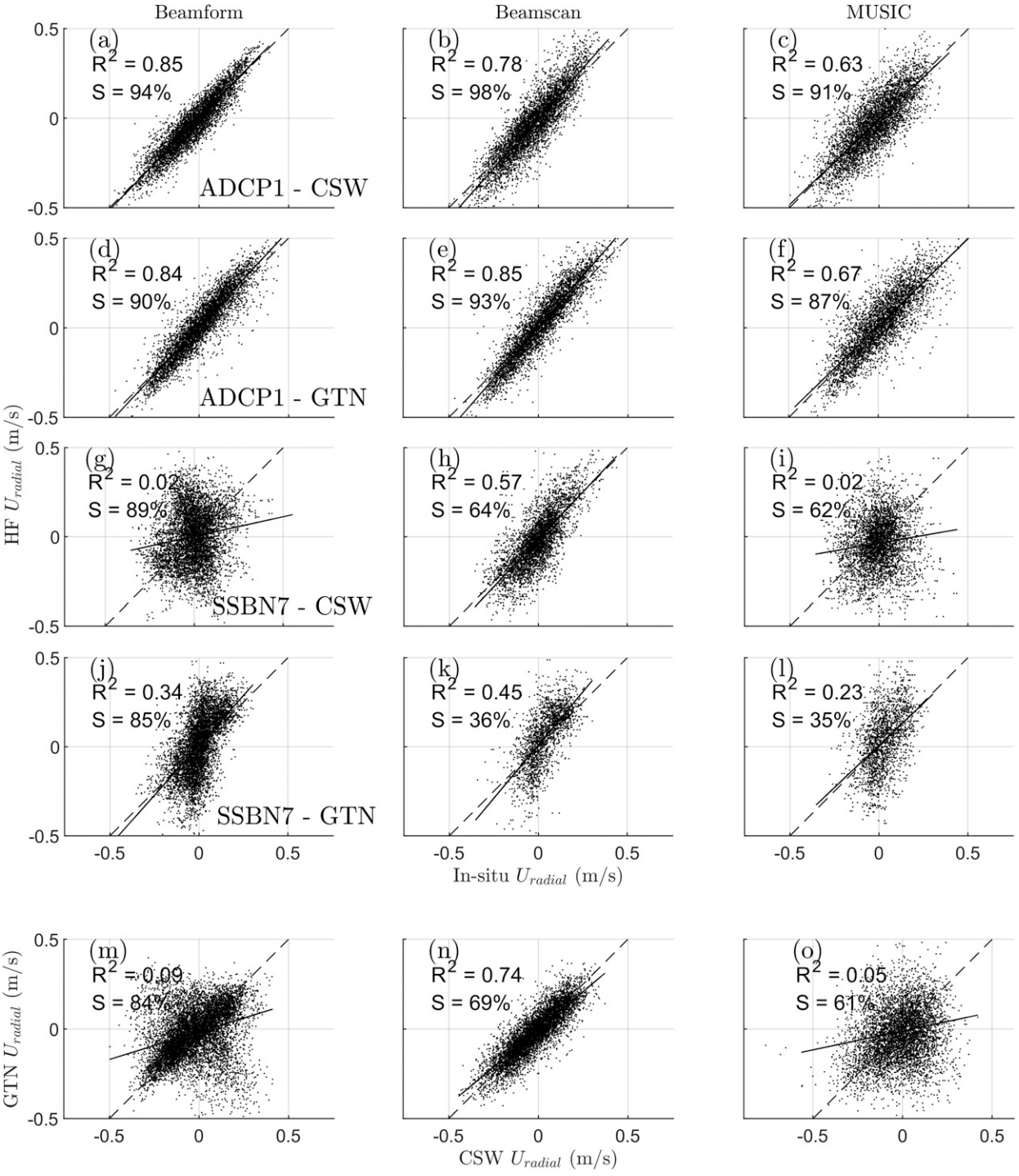

FIG. 10. Scatter diagrams of HF radar radial velocity estimates derived using the (left) beamforming, (center) Beamscan, and (right) MUSIC methods against (a)–(l) in situ measurements and (m)–(o) MDPT. The linear regression and the 1:1 lines are shown as solid and dashed lines, respectively. The *S* values represent the percentage of time each particular method provided a solution.

of the method used. At MDPT and SSBN7 beamforming has the lowest correlation for all events. On average, at SSBN7, Beamscan and MUSIC perform similarly while at MDPT Beamscan performs better than MUSIC.

Event C is most representative of the climatological average with winds stronger offshore and wave heights larger offshore (Wu et al. 2018) and it is selected for a more detailed examination. Time series of the radial current estimates during event

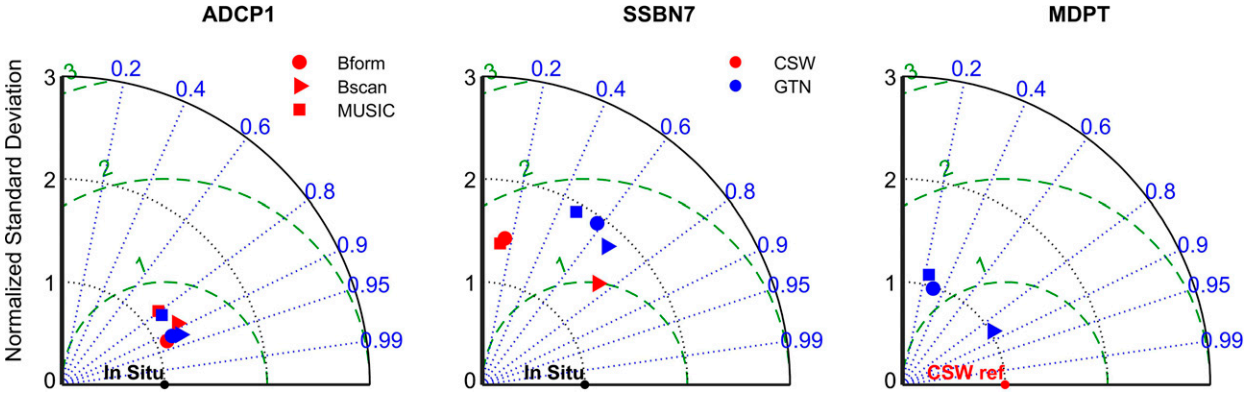

FIG. 11. Taylor diagrams for radial current comparisons from 1 Jul 2016 to 31 Jan 2017 at sites (left) ADCP1, (center) SSBN7, and (right) MDPT. Normalized RMSD is shown as the dashed green lines.

C, from each method and location, are shown in Fig. 13. At ADCP1, all three HF radar methods agree well with the in situ measurements (see Figs. 13a,b) as indicated by the good correlations found (Fig. 12, left column). The tidally modulated current is clearly seen in the HF radar surface current estimates in agreement with the in situ records. At SSBN7 and MDPT, MUSIC and Beamscan are noisy (Figs. 13c–g) while the beamforming estimates at SSBN7 clearly capture a tidal modulation (red line in Fig. 13c) as it was the case at ADCP1.

The performance of the three methods at MDPT are shown in Figs. 13e–g. Beamforming (Fig. 13e) estimates from the two radar sites are not consistent. At this location both systems should be reporting identical currents but instead the estimates, although they capture a tidal signal, appear to be out of phase for a good part of the record. However, Beamscan (Fig. 13f) and MUSIC (Fig. 13g) show better agreement with each other. For both Beamscan and MUSIC the errors in velocities seem random.

e. *Effect of beamforming's beam pattern*

Beamforming creates a "beam" in the direction of the intended measurement direction [see (6)]. Theoretically, the beam pattern is narrow (15°beamwidth along the radar boresight) for a 12 antenna linear array with half wavelength spacing and the sidelobe suppression is ~40 dB. Figure 14 shows theoretical beam patterns for the 12 antenna receiving arrays (CSW and GTN), pointed toward the three measurement locations. Although the beamwidth is significantly larger at the direction toward SSBN7 (Figs. 14c,d: steering angle = 59.1° and −47.9° for GTN and CSW, respectively) than at ADCP1 (Figs. 14a,b: steering angle = 9.4° and −4.9° for GTN and CSW, respectively), the sidelobes are suppressed by almost 40 dB in both cases.

According to radar theory, the signal scattered from Bragg waves is proportional to the Bragg wave height along the radar site radial direction (Barrick 1972). The beamformed Doppler spectrum at a certain range (r), and steering angle (θ_{st}) is a convolution of the RX beam pattern [$B_{r,\theta_{st}}(\theta)$], where θ is measured from the radar boresight, and the Bragg wave height $H_B(r, \theta)$ along the semicircle with a radius r. If we consider the theoretical beam patterns shown in Figs. 14a–d, the Bragg wave height would have to be 20 dB higher (giving a 40 dB difference in the radar cross section) somewhere along the semicircle of range r to overpower the sidelobe suppression. This would result in the beamformed Doppler spectrum containing information from this unintended direction. In most environments this is not expected to impact a beam forming radar system with 12 antennas if they perform as theory suggests (Laws et al. 2000). However, real antenna patterns often deviate from the theoretically estimated ones. Gurgel et al. (1999) has shown that for a linear array a variation in distance from the waterline along the RX array can

TABLE 3. HF radar comparison statistics: slope (s), bias (in cm s^{-1}), correlation coefficient (R^2), RMSD (in cm s^{-1}), and NMRSD for the different methods of radar signal analysis.

		Beamforming					Beamscan					MUSIC				
Site	Radar	s	Bias	R^2	RMSD	NRMSD	s	Bias	R^2	RMSD	NRMSD	s	Bias	R^2	RMSD	NRMSD
ADCP1	CSW	0.99	−0.2	0.79	7.0	0.50	1.1	−1.6	0.8	7.7	0.55	1.1	−0.15	0.78	8.1	0.58
	GTN	1.1	1.4	0.79	8.5	0.57	1.1	0.3	0.85	7.1	0.48	1.1	0.5	0.84	7.2	0.48
SSBN7	CSW	0.04	0.8	0	16	1.32	0.99	−1.2	0.52	9.3	0.94	0.92	−0.8	0.42	9.9	1.1
	GTN	1.06	0.9	0.29	14	1.64	1.1	0.1	0.32	13	1.64	1.04	1.1	0.27	13	1.7
MDPT		0.06	−2.2	0.01	14	—	0.89	−0.3	0.76	6.4	—	0.49	−0.2	0.37	10	—

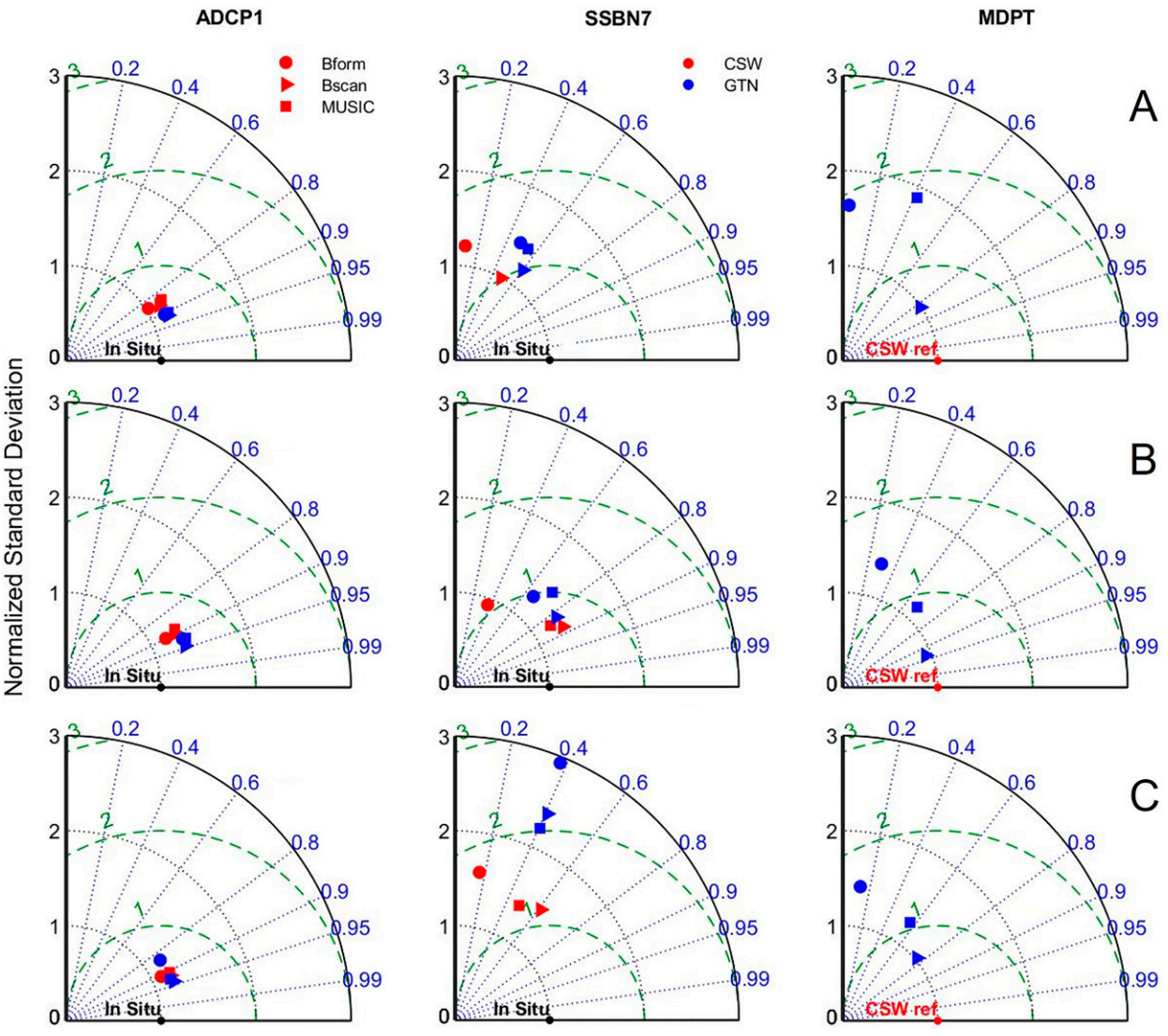

FIG. 12. Taylor diagrams for radial current comparisons during events A–C that correspond to the different time periods shown in Fig. 6.

reduce sidelobe suppression by 15 dB. Preliminary antenna pattern measurements in CSW using a small quadcopter (Cahl and Voulgaris 2016) suggested significantly higher sidelobes than the theoretically predicted.

In addition, the four-element transmit array used in WERA systems is a rectangular array that directs most of the radar signal toward the ocean with an approximately 80° beamwidth (see Figs. 14e,f). Multiplying the TX and RX pattern results in an effective beam pattern, shown as the solid lines in Fig. 15. For location ADCP1 the effective beam patterns have smaller sidelobes by a few decibels while at location SSBN7 the sidelobes are increased by 5 and 10 dB for CSW and GTN, respectively.

Furthermore, the performance the RX array as a whole depends on the quality of the individual antenna elements. At CSW, antenna 3 had little to no signal for the first half of the study period. After antenna 3 was fixed, antenna 8 was damaged and had little to no signal for the second half of the study period (see Fig. 9). At GTN, antennas 5 and 7 were damaged and exhibited low SNR during event C (see Fig. 8). The effects of reduced antenna element performance are assessed by calculating effective beam patterns (including the effect of the TX pattern) with the malfunctioning antennas removed. With antennas 3 and 8 removed (see Fig. 15) the change in the effective beam patterns is similar for CSW and GTN. This modification results in reduced sidelobe suppression of 30 and 20 dB, respectively for site ADCP1 and 20 and 10 dB for SSBN7.

This reduced sidelobe suppression suggests that beamforming measurements at SSBN7, with antenna 8 performing poorly at CSW, would be inaccurate if the Bragg wave height varies by more than a factor of $\sqrt{10} \cong 3.3$ (since the radar cross section is proportional to spectral energy, or wave height squared) along the semicircle corresponding to the range of SSBN7 from site CSW. This sidelobe suppression of only 10 dB could allow the Bragg scattered HF radar signal

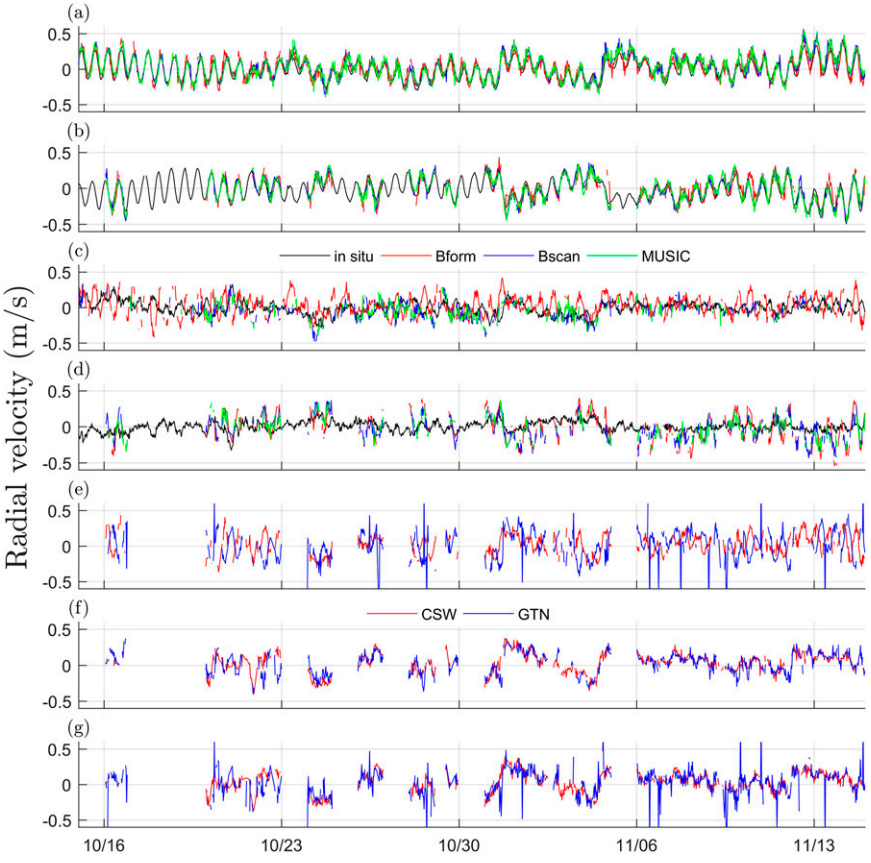

FIG. 13. Event C time series of in situ and HF radar surface currents obtained with the three different methods of analysis (beamforming, Beamscan, and MUSIC shown in red, blue, and green lines, respectively). (a) GTN and (b) CSW for offshore site ADCP1; (c) GTN and (d) CSW for nearshore site SSBN7. The radial currents from CSW (red line) and GTN (blue line) for MDPT for (e) beamforming, (f) Beamscan, and (g) MUSIC.

from other directions to overwhelm the beam pattern steered toward to SSBN7.

f. Theoretical evaluation of beamforming and Beamscan

In this section beamforming and Beamscan are evaluated using the method of Wang and Gill (2016). Modeled Doppler spectra for each HF radar antenna are created and then surface current analysis is carried out on these theoretical spectra. Wang and Gill (2016) evaluated MUSIC versus beamforming, but they did not use the directional characteristics of the TX array, something that is included in here.

For a single range bin, prediction of the Doppler spectrum for each antenna requires knowledge of the wave and current fields at every point along the range ring. Since wave and current information exist only for two locations in this study (ADCP1 and SSBN7), full Doppler spectrum estimation for each antenna is not possible using in situ data. Therefore, an idealized EM backscattering model is used to estimate Doppler spectra in each antenna (for a single range bin) using two different surface current scenarios. Subsequently, Beamscan and beamforming is performed to estimate surface currents, which are compared to the surface current inputs of the model.

The Wang and Gill (2016) model used here simulates the first-order spectrum (Bragg peak) and does not consider second-order effects. The model estimates the signal in each antenna j by summing the signal received from each radial direction θ from the boresight:

$$s(t)_j = \sum_{\theta}[A_p(\theta)e^{2\pi i(f_B+f_c)t} + A_n(\theta)e^{-2\pi i(f_B-f_c)t} + \phi_j(\theta)] + \text{noise}, \tag{12}$$

where f_B is the Bragg frequency and f_c is the Doppler shift due to the radial current $u_r(\theta)$. The phase shift ϕ_j for each antenna j is given by (5). The spectral amplitudes of Bragg waves traveling toward and away from the radar are represented by A_p and A_n, respectively. This idealized model assumes a fully developed sea where the Bragg wave spectral energy $[S_w(f_B, \theta)]$ is determined by the directional characteristics of the wave field, which is assumed to be $\cos^4$ (e.g., Longuet-Higgins 1962):

$$S_w(f_B, \theta) = S_w(f_B)\cos^4\left(\frac{\theta - \theta_w}{2}\right) + 0.01, \tag{13}$$

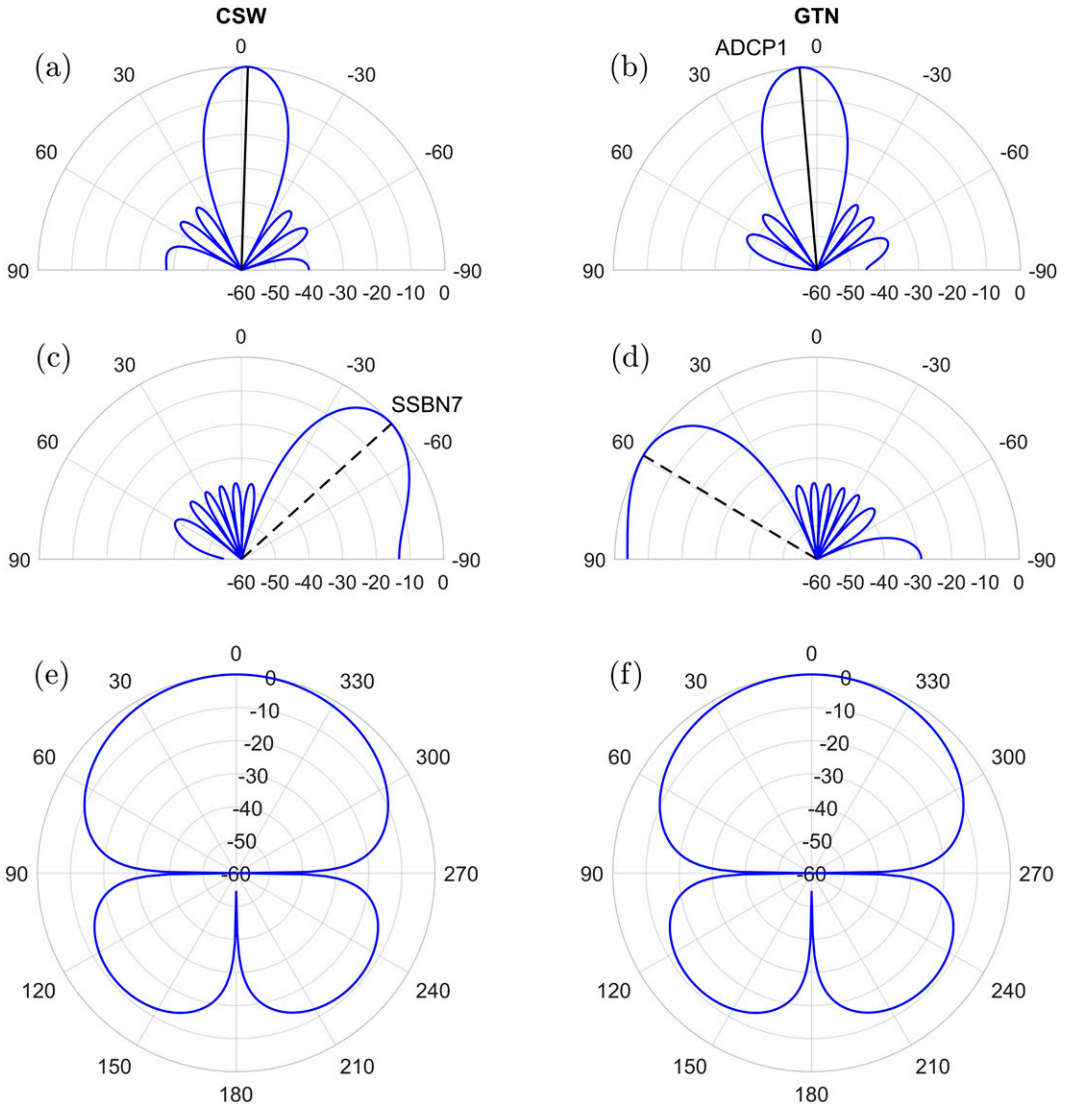

FIG. 14. (a)–(d) Theoretical RX beam patterns for a 12-antenna linear array with 0.45λ antenna spacing using a Hamming window and for steering angles corresponding to those toward the comparison sites. (a) CSW-ADCP1 (steering angle $\theta_{st} = -4.9°$); (b) GTN-ADCP1 ($\theta_{st} = 9.4°$); (c) CSW-SSBN7 ($\theta_{st} = -47.9°$); (d) GTN-SSBN7 ($\theta_{st} = 59.1°$). Theoretical transmit patterns for (e) CSW and (f) GTN using idealized antenna positions for the TX arrays (0.5$\lambda \times$ 0.15λ spacing with a phase delay of 0.35λ for the rear antennas).

where the wind direction is given by θ_w and θ is the angle measured from the boresight.

The synthetic signal (12) generated consists of 2048 samples with a chirp length of 0.433 33 s (the same as the radar system used in this study). Random Gaussian noise is added to the signal so that the SNR of the larger Bragg peak to the noise in the Doppler spectrum [the Fourier transform of $s(t)_j$] is either 20 dB (high-SNR case) or 10 dB (low-SNR case). For the model runs discussed here, the wind direction is directed toward the radar site, along the radar boresight and the beam patterns are those shown in Figs. 14 and 15.

Two synthetic current flows were considered, similar to Wang and Gill (2016): (i) a constant speed current flowing parallel to the coast, depicted in Fig. 16 (top) and (ii) a parallel current to the coast as in (i) with large cross-shore flow (i.e., river outflow) depicted in Fig. 17 (top). In the latter case, this "burst" or cross-shore flow resembles a Gaussian distribution of radial velocity with the peak speed located at $\theta = -20°$ (Fig. 17a). After the modeled signals (12) and corresponding Doppler spectra are created, Beamscan and beamforming (as described in section 3) are used to estimate radial currents. As in Wang and Gill (2016), this is repeated 100 times for each method and then the estimated radial currents are bin averaged (1° bin size) radials current estimates are shown in Figs. 16a–d and 17a–d.

For a uniform current profile both Beamscan and beamforming estimates agree well with the synthetic flow when not

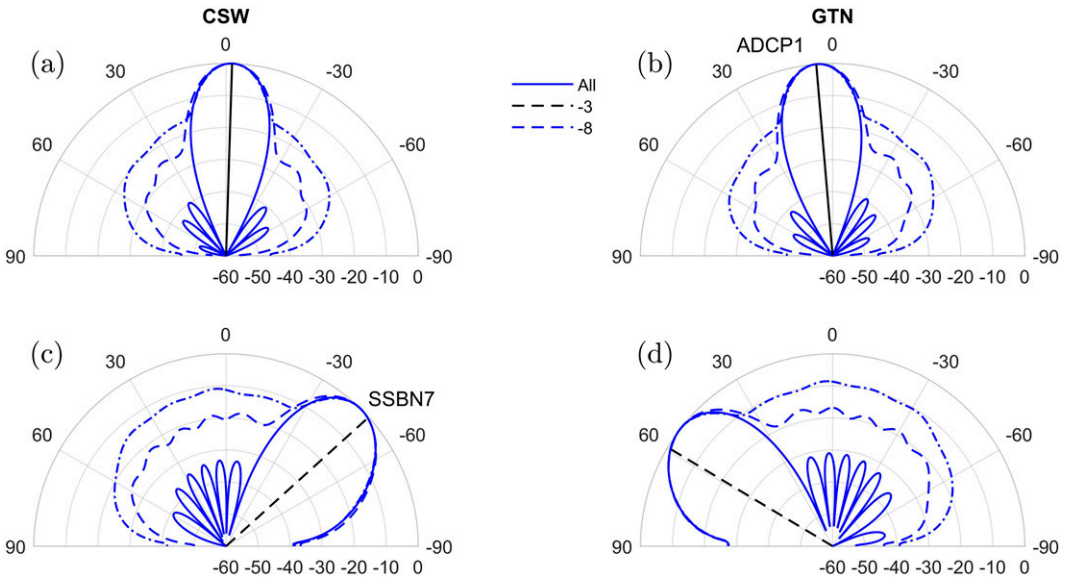

FIG. 15. Theoretical beam patterns for a 12-antenna array after accounting for the TX antenna pattern (see Figs. 14e,f). (a) CSW-ADCP1 ($\theta_{st} = -4.9°$); (b) GTN-ADCP1 ($\theta_{st} = 9.4°$); (c) CSW-SSBN7 ($\theta_{st} = 47.9°$); (d) GTN-SSBN7 ($\theta_{st} = -59.1°$). Solid lines show the effective beam pattern when all antennas are functioning. Dashed and dash–dotted lines show the pattern with antenna 3 and antenna 8 removed, respectively. Solid black lines denote the direction toward ADCP1 while the dashed black lines denote the direction toward SSBN7.

accounting for the transmit pattern (Figs. 16a,b). When accounting for the transmit pattern, Beamscan performs well in both the low- and higher-SNR cases (Figs. 16c,d) but fails to produce results for beam angles greater than 50° in the low SNR case. For beamforming, the low-SNR case (Fig. 16d) has large inaccuracies at beam angles > 40° while the deviations at these high angles are smaller for the high-SNR case (Fig. 16c).

For the Gaussian "burst" profile (Fig. 17), Beamscan performs well in all cases and captures the Gaussian profile almost completely. However, it does not return current estimates at beam angles > 50° in the low-SNR case when accounting for TX (Fig. 17d). Beamforming does identify the Gaussian current profile for all cases but only at roughly half the amplitude of the model input Gaussian. As described earlier when accounting for TX, beamforming estimates deviate from the synthetic ones at higher radial angles and the deviation is bigger for lower SNR (Figs. 17c,d).

The results here show Beamscan to be better than beamforming in capturing the Gaussian burst current profile, which is similar to the results of Wang and Gill (2016) that found MUSIC to outperform beamforming in these cases. Additionally, when accounting for the transmit pattern, we find that at high beam angles beamforming produces less accurate results while Beamscan is less likely to produce results especially at low-SNR cases. It should be noted that in all cases the wind was directed toward the radar boresight.

5. Discussion

Source of radial estimates errors

Intrinsic angular biases are known to exist in both DF- CCL systems and BLA radar systems (Emery et al. 2004; Cosoli and de Vos 2019). A similar analysis is done here for location ADCP1 using beamforming, Beamscan, and MUSIC (see Fig. 18). The radial HF radar currents are compared to the in situ radial currents at ADCP1 for different bearing angles of the radar. The true direction of ADCP1 is shown as the gray dashed line in Fig. 18. For CSW, both R^2 and RMSD values show the best correlations and minimum difference with the in situ data at angles within 2° of the true direction (Figs. 18a,b) for all methods. At GTN, the best correlation (R^2) with the in situ data is within 2° in bearing direction from the true direction of ADCP1 using any method (Fig. 18c) while the best RMSD values are within 4° (see Fig. 18d). It should be noted here that the direction finding methods decorrelate faster than beamforming, especially for CSW (Figs. 18a,b).

Overall, our HF radar measurements corresponding to SSBN7 and MDPT, the two locations with high steering angles, show that although MUSIC performs better than beamforming, Beamscan outperforms both methods (see Figs. 9–11).

The beamforming radial current estimates at both MDPT and SSBN7 exhibit tidal variability that is similar to that found at ADCP1 during event C (Fig. 13) something unexpected given the relative position of the two stations in relation to the coastline. This is not the case for the MUSIC and Beamscan radial current estimates. As discussed in section 3b(2), in contrast to beamforming, both Beamscan and MUSIC first separate the Doppler spectrum into separate frequency bins and subsequently try to identify the direction of arrival of each frequency. Separating the signal first by frequency may suppress stronger signals at other frequencies more than beamforming as the latter relies solely on the beam pattern for suppression. The

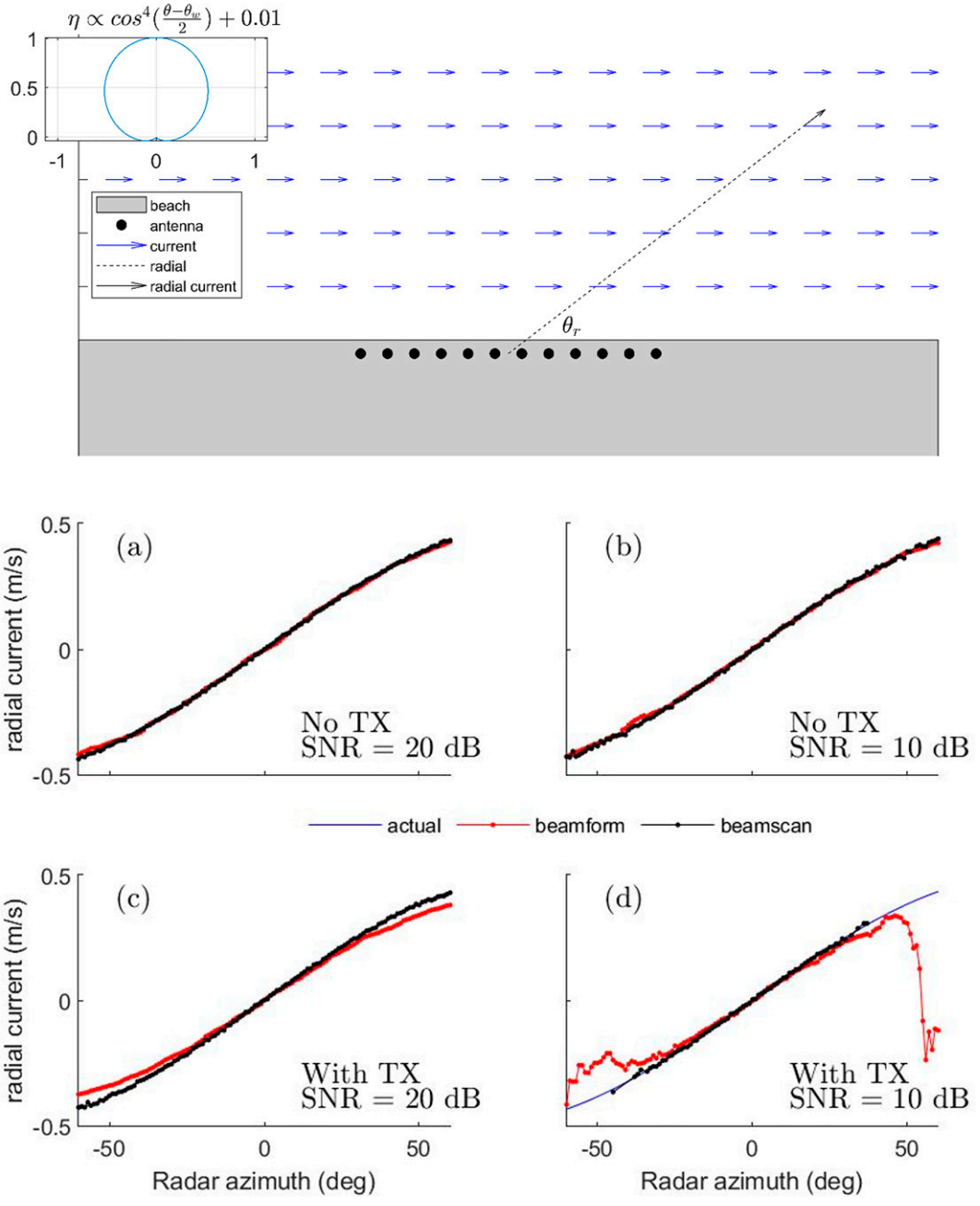

FIG. 16. (top) Schematic of flow conditions for the constant-current-profile case used to drive the HF radar forward model. (bottom) Comparison of Beamscan and beamforming current estimates (a),(b) without and (c),(d) with TX pattern included and for high (20 dB) and low (10 dB) SNR.

effective beam patterns at SSBN7 (Figs. 15c,d) have sidelobes that are not well suppressed when one of the antennas is not operational. Under such circumstances, a strong signal from a different location would not be sufficiently suppressed and could overwhelm the signal from SSBN7.

Although the theoretical beam patterns presented in here are smooth, real antenna patterns are known to be noisier due to antenna geometry imperfections and local environmental conditions potentially reducing the effectiveness of sidelobe suppression. This would lead to the HF radar beamformed current estimates at SSBN7 to reflect ocean current values corresponding to a different patch of the ocean but of the same range. If this is the case, the tidal characteristics of the beamformed radial estimates at SSBN7 should match those at a different location of the ocean. This is further explored below. Additionally, it should be noted that MUSIC is known to be

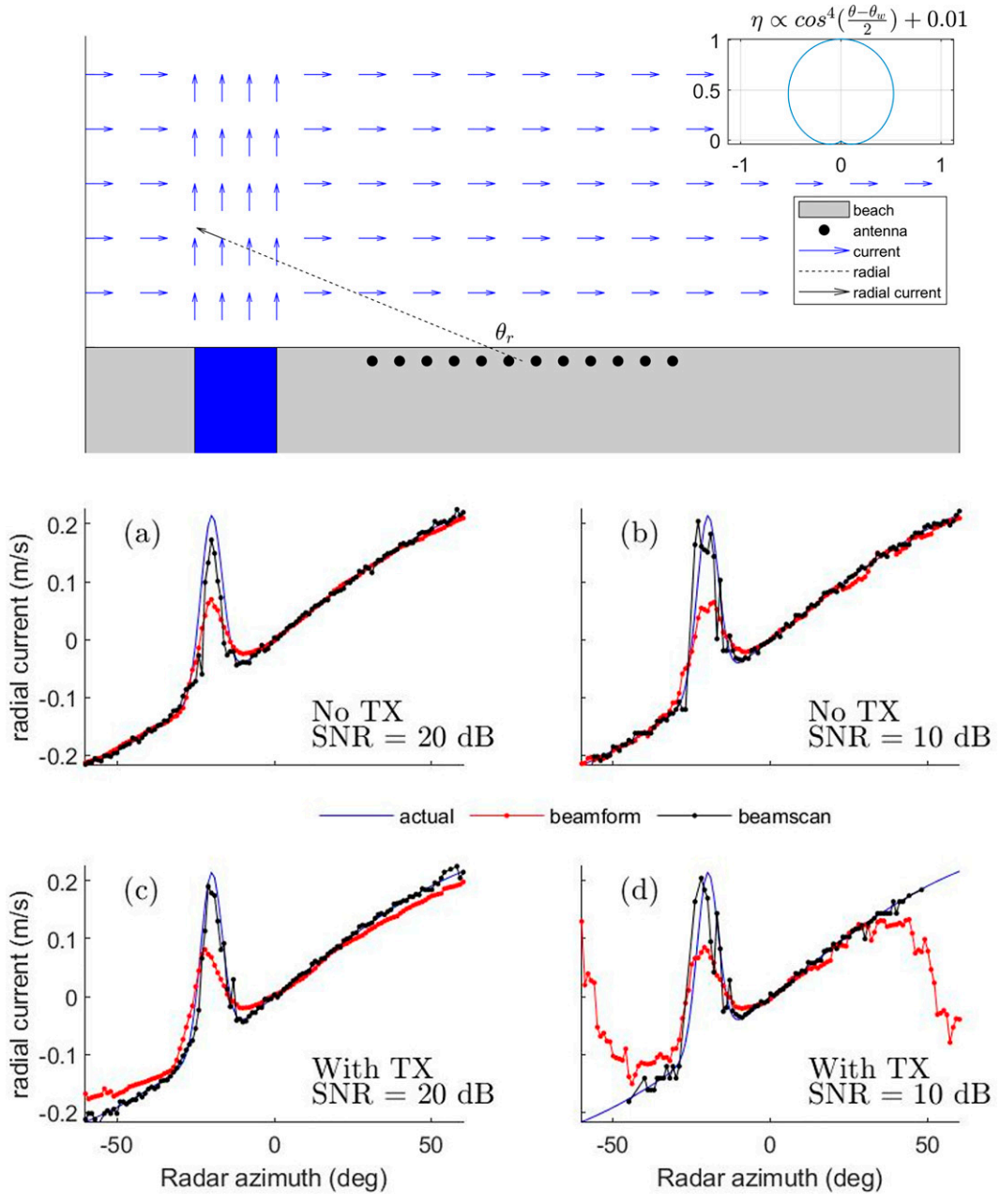

FIG. 17. (top) Schematic of flow conditions for the Gaussian radial current profile case used to drive the HF radar forward model. (bottom) Comparison of Beamscan and beamforming current estimates (a),(b) without and (c),(d) with TX pattern included and for high (20 dB) and low (10 dB) SNR.

sensitive to imperfections in antenna patterns (Dumas and Guérin 2020).

1) TIDAL ANALYSIS

As noted earlier tidal flows in Long Bay are dominated by semidiurnal tides (Blanton et al. 2004; Gutierrez 2006). Therefore, we use this tidal signal to identify the discrepancies observed in the current estimates. Harmonic analysis (Pawlowicz et al. 2002) was carried out on the in situ and radar derived radial velocities estimated using the different methods at the various stations using the full time series available. The results for the dominant constituent (M_2) are listed in Table 4 and suggest that at the offshore site (ADCP1, low steering angle) the in situ and radar methods are within 3 cm s^{-1} in amplitude and 12° in phase values (see Table 4). The tidal analysis for SSBN7 shows that the M_2 characteristics derived from Beamscan and MUSIC are much closer to the in situ results than beamforming.

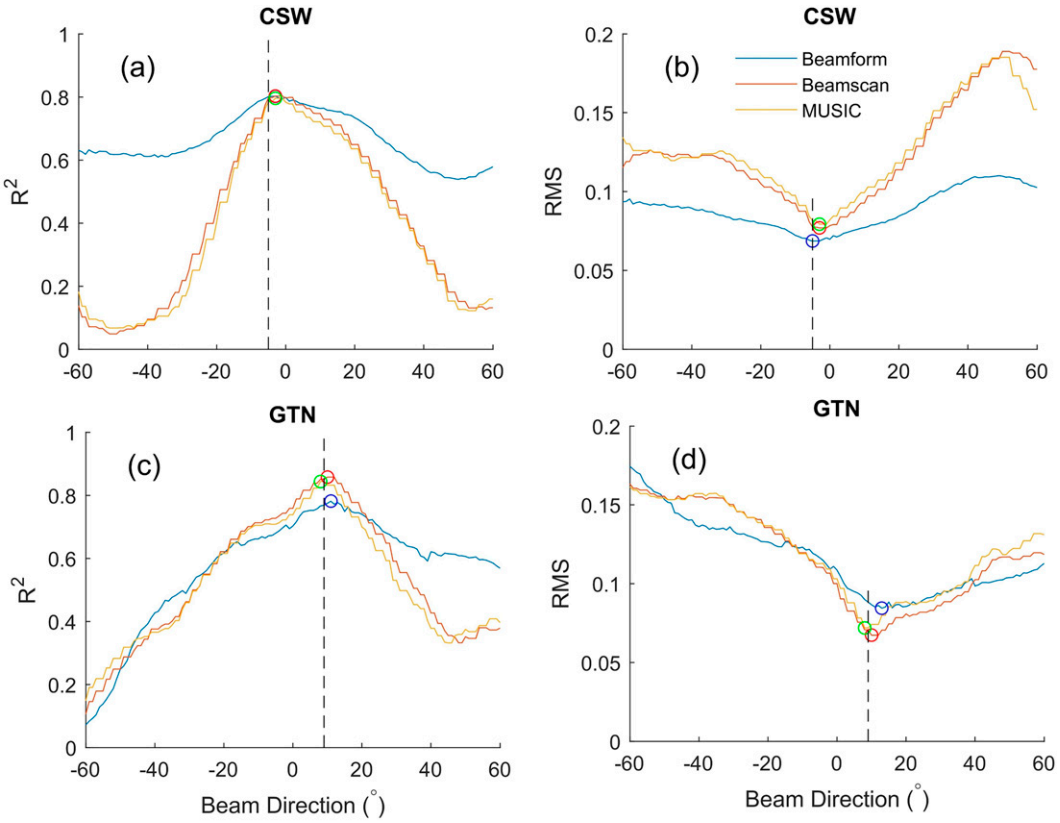

FIG. 18. The correlation (R^2) and RMSD between HF radar radial current estimates and in situ radial currents at ADCP1 for different radial directions. The vertical dashed line indicated the true direction of the in situ location. Beamforming's (blue), Beamscan's (red), and MUSIC's (yellow) best correlations and minimum in RMSD is shown as circles.

2) SOURCE (AZIMUTH) OF THE BACKSCATTERED SIGNAL

To estimate the origin (azimuth) of the backscattered signal that leads to the radar derived radial currents (and therefore the radar derived M_2) at each station, an optimization method is utilized. The assumption is that the source of the signal is located at the same range as the intended station, but at a different azimuth. The optimization method identifies an azimuth on this range ring where the HF radar derived M_2 amplitude and phase (Table 4) match modeled barotropic tides at this location [available at https://adcirc.org/products/adcirc-tidal-databases/; see Blanton et al. (2004) and Szpilka et al. (2016) for details]. The minimization process includes both normalized velocity and phase errors $E(\theta)$ and it is defined as the difference (RMSD) between the radar estimated tidal harmonic and the modeled tidal harmonic projected onto the radar radial over one tidal cycle:

$$E(\theta) = \frac{1}{2\pi}\int_0^{2\pi} \{\upsilon_{\mathrm{HF}}\sin(t + \phi_{\mathrm{HF}}) - \upsilon_{\mathrm{DB}}(\theta)\sin[t + \phi_{\mathrm{DB}}(\theta)]\}^2 dt, \tag{14}$$

where $\upsilon_{\mathrm{HF}}(0)$, $\phi_{\mathrm{HF}}(0)$, and $\upsilon_{\mathrm{DB}}(\theta)$, $\phi_{\mathrm{DBm}}(\theta)$ are the M_2 amplitude and phase, from the HF radar and tidal database, respectively; θ is the radial angle with $\theta = 0$ defined as the direction of the HF radar toward the location the optimization method is applied (e.g., ADCP1). t in (14) denotes tidal phase within the M_2 tidal cycle. The value $\Delta\theta$ where the function $E(\theta)$ in minimized is assumed to represent the azimuth that the signal comes from, and it represents the difference in direction between the intended beam direction and the location the tidal analysis from the HF radar measurement that most closely matches the model.

Application of the optimization method to the offshore site ADCP1 is shown in Fig. 19a where the range rings for that site corresponding to CSW and GTN radar systems are shown as dotted black lines. The $\Delta\theta$ values for the HF radar derived M_2 radial amplitudes/phases are listed in Table 4 and shown on the ADCP1 range rings in Fig. 19. At ADCP1, $\Delta\theta$ for CSW, when compared to the modeled tides are low ($\Delta\theta \leq 5.4°$ for all three methods), which agrees with the comparison of the in situ measurements and the modeled tides ($\Delta\theta = 5.4°$). For GTN, in situ azimuth error ($\Delta\theta = -3.6°$) differ by less than 15° to the radar results, beamforming ($\Delta\theta = -18°$), Beamscan ($\Delta\theta = -12.6°$), and MUSIC ($\Delta\theta = -12.6°$). In Fig. 19a, the differences to the model ($\Delta\theta$) are plotted and the in situ measurements and all three radar methods closely agree for CSW. At GTN, the differences between the radar and in situ data are equal to roughly half the beamwidth (15°) and therefore within

TABLE 4. Amplitude and phase of the M_2 constituent estimated using the different radar radial velocity components at the different locations (ADCP1, SSBN7, and MDPT). $\Delta\theta$ is the result of the optimization method used to identify the source of the signal (see text for details).

Location	Radial velocity	Radial direction	Amplitude (cm s^{-1})	Phase (°)	$\Delta\theta$ (°)
ADCP1	In situ	CSW	12.7 ± 0.2	125.9 ± 1.1	5.4
		GTN	13.1 ± 0.3	55.4 ± 1.2	−3.6
	Beamform	CSW	12.5 ± 0.2	121.9 ± 1.1	5.4
		GTN	16.1 ± 0.3	67.2 ± 1.2	−18
	Beamscan	CSW	12.2 ± 0.3	137.9 ± 1.2	−1.8
		GTN	15.2 ± 0.2	61.3 ± 1.1	−12.6
	MUSIC	CSW	12.4 ± 0.3	139.0 ± 1.3	−1.8
		GTN	14.8 ± 0.3	61.3 ± 1.1	−12.6
SSBN7	In situ	CSW	5.1 ± 0.3	280.5 ± 3.5	−1.8
		GTN	2.3 ± 0.3	101.5 ± 7.5	−1.8
	Beamform	CSW	12.1 ± 0.6	112.9 ± 2.7	64.8
		GTN	11.9 ± 0.5	70.3 ± 2.4	−41.4
	Beamscan	CSW	3.8 ± 0.4	274.9 ± 5.5	0.0
		GTN	6.8 ± 0.4	86.7 ± 3.4	−1.8
	MUSIC	CSW	1.7 ± 0.4	273.3 ± 13.4	−1.8
		GTN	7.6 ± 0.4	84.6 ± 2.5	1.8
MDPT	Beamform	CSW	10.4 ± 0.4	112.9 ± 1.9	37.8
		GTN	10.4 ± 0.7	250.1 ± 3.9	14.4
	Beamscan	CSW	4.7 ± 0.3	233.4 ± 3.1	−3.6
		GTN	4.8 ± 0.4	233.6 ± 4.8	−16.2
	MUSIC	CSW	4.8 ± 0.4	240.0 ± 3.6	−5.4
		GTN	4.3 ± 0.5	245.5 ± 6.8	14.4

expected accuracy. Therefore, HF radar measurements at ADCP1 fall within the expected azimuth accuracy.

Similar analysis was carried for the nearshore station SSBN7 and the location MDPT along the baseline. The error in azimuth ($\Delta\theta$) at these two locations are shown in Table 4 and are plotted along the range rings in Figs. 19b and 9c. At SSBN7 (Fig. 19c) the in situ, Beamscan, and MUSIC errors in azimuth are within 2° of the modeled tides. However, the beamforming errors in azimuth are over 40° for both CSW and GTN. As seen in Fig. 19c, the actual directions the beamformed and MUSIC tidal signals come from are closer to the radar boresight than the intended beam direction.

At MDPT (Fig. 19b), the errors in azimuth are below 20° for Beamscan and MUSIC while beamforming has an error of 37.8° for CSW. Although the errors in azimuth are similar for beamforming at GTN, the difference in tidal amplitude is large; close to the in situ tidal amplitude at ADCP1.

$\Delta\theta$ suggests that the beamformed error in direction ranges from 0° to 64.8° in this study. This error in direction is greater than half the beamwidth and is most likely due to sidelobe contamination as can be expected from our previous considerations of the beam pattern and HF radar forward modeling (Figs. 16 and 17). This large bias in direction is unwanted but does explain why we see such large tidal modulation in the beamformed currents (Figs. 13c–e).

6. Summary and conclusions

While numerous studies have focused on evaluating the performance of HF radar systems with in situ data, most have concentrated on establishing the accuracy of the radars. In this study we examined the potential reasons a HF radar system might not perform as expected and we identified alternative methods to analyze the signal as to improve performance. We compared HF radar surface currents to in situ measured currents from two linear HF radar arrays under normal operational conditions and at large steering angles, with and without malfunctioning antennas. HF radar surface currents were estimated using beamforming (the standard method for linear arrays) and two direction finding methods: the commonly used algorithm, MUSIC, and Beamscan. Our results indicate that all three HF radar methods perform well at low azimuth angles (i.e., close to the radar boresight). This location is representative of how beamforming performs when the beampattern suppresses sidelobes well.

However, at locations far from the radar boresight (steering angle $> 35°$) beamforming was found to be a poor performer for our system (RMSD and NRMSD of roughly 14–16 cm s^{-1} and 1.5, respectively); Beamscan and MUSIC show better correlation with in situ data at location SSBN7 corresponding to a large steering angle. For Beamscan and MUSIC, RMSD values are 9–13 cm s^{-1}. At the baseline midpoint (steering angle of 38°), the two radars correlate to each other significantly better using Beamscan ($R^2 = 0.76$, RMSD = 6.4 cm s^{-1}) than either beamforming ($R^2 = 0.01$, RMSD = 14 cm s^{-1}) or MUSIC ($R^2 = 0.49$, RMSD = 10 cm s^{-1}), although MUSIC still performs much better than beamforming.

Notably, when all antennas are functioning well (site GTN for events A and B) beamforming performed similarly to

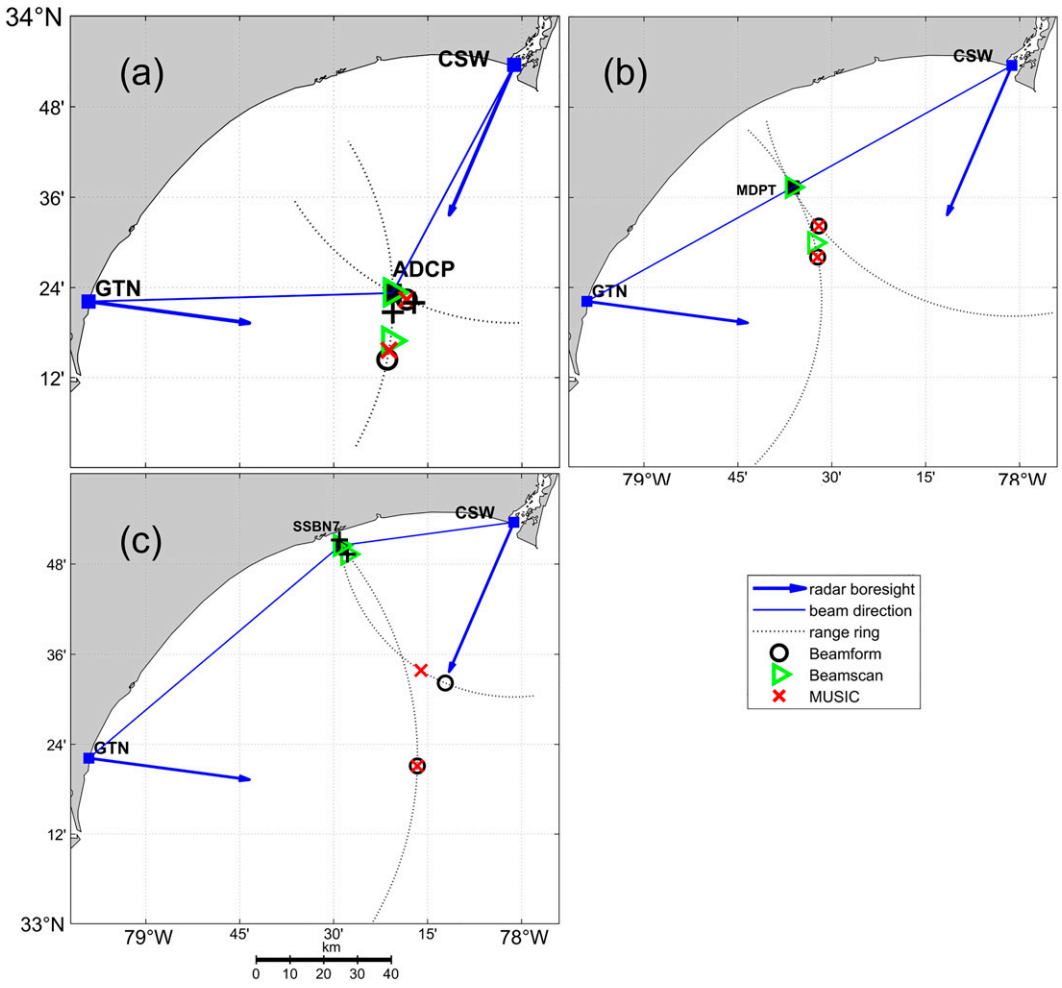

FIG. 19. Results of the minimization analysis (see text for details) performed to the tidal M_2 signal recorded on sites (a) ADCP1, (b) MDPT, and (c) SSBN7. In each panel a black + symbol is used to mark the location along the range circle where the in situ radial amplitude and phase match those of the model. Locations where beamforming- (black circles), Beamscan- (green triangle), and MUSIC- (red × symbols) derived radial current solutions match those of the tidal model. The radar boresight and beam direction are shown with blue arrows and blue lines, respectively.

Beamscan during event A at both locations (SSBN7 and MDPT); however, wave height was higher at SSBN7 than near the GTN boresight (ADCP1) during this time. During event B, which better represents climatological averages where wave height is lower nearshore (SSBN7) than offshore (ADCP1), Beamscan performed better than beamforming even though all antennas were functioning well for site GTN. During the other events and for site CSW, not all antennas were functioning correctly, which caused a significant degradation in the beam pattern. For these situations, Beamscan performed significantly better than beamforming. Although these antennas can be fixed, an eight-antenna linear array always has lower sidelobe suppression, and therefore, Beamscan may offer better performance than beamforming at large steering angles on these systems.

Besides the known degradation of the beam pattern at large angles from the boresight, the additional effects of the transmit pattern significantly effect beamforming in our modeled results, especially with low SNR. The transmit pattern will vary with other TX array configurations and we suggest future research incorporates TX array characteristics (including measuring the transmit beam pattern) in HF radar modeling. As in the modeled results, the HF radar measurements near the coast (SSBN7 and MDPT) resulted in beamformed currents with low accuracy when wave height was significantly higher offshore (in the direction of the radar boresights). Under such conditions comparing the results with those obtained using a direction finding method might be beneficial as the latter method would provide data that are in disagreement to the beamforming data. This could be recorded as a flag alerting the operator that these locations may be problematic.

At SSBN7 and MDPT, where wave energy is low and the beam pattern is poor, the direction finding methods' results are noisy, while the beamformed current estimates have tidal

modulation resembling the beamformed measurements closer to the radar boresight. Tidal analysis of the HF radar radials currents confirms these expectations. The beamformed HF radar measurements do not agree with in situ measurements at the high steering angles (SSBN7) but instead agree with the modeled tides from an offshore location much closer to the radar boresight. In a worst-case scenario, the pointing error in beamforming was over 60° (see Table 4). The random errors in Beamscan do not affect tidal analysis, and HF radar derived tidal M_2 constituents closely matches the in situ derived results and the modeled tides at this high steering angle location.

The Beamscan direction finding method used here could be easily applied to beamforming HF radar systems operationally as it does not require extensive tuning and more easily adaptable for longer term operations where antenna characteristics tend to deteriorate over time. Disagreements between the two solutions can be used to identify possible issues in beamforming at particular locations in the HF radar coverage area. The Beamscan direction finding along with the beamforming and MUSIC MATLAB codes used here are available in Cahl and Voulgaris (2022), while codes for reading WERA raw data are available in Voulgaris and Cahl (2020).

Acknowledgments. Support during data analysis and preparation of this manuscript was provided by the Southeast Coastal Observing Regional Association (SECOORA) pursuant to NOAA Award NA16NOS0120028. Revisions and finalization of the manuscript took place while George Voulgaris was serving at the National Science Foundation. The contribution of the three anonymous reviewers in improving earlier versions of the manuscript is greatly acknowledged.

Data availability statement. This publication is supported by multiple datasets. Most in situ measurements and the model tidal database are openly available at the locations cited in the text and references. The in situ measurements for site ADCP1 were collected by Lynn Leonard (lynnl@uncw.edu) at the University of North Carolina Wilmington. In situ current data from the ADCP and HF radar radial current data used during this study are openly available from https://doi.org/10.5281/zenodo.7236610. HF radar analysis codes in MATLAB are available at https://doi.org/10.5281/zenodo.7230998. Raw Doppler spectra from the two HF radar sites are not archived publicly due to the large size (>1 TB) but are available from the HF radar site operator George Voulgaris (gvoulgaris@geol.sc.edu) at the University of South Carolina.

REFERENCES

Abascal, A. J., S. Castanedo, R. Medina, I. J. Losada, and E. Alvarez-Fanjul, 2009: Application of HF radar currents to oil spill modelling. *Mar. Pollut. Bull.*, **58**, 238–248, https://doi.org/10.1016/j.marpolbul.2008.09.020.

Barrick, D. E., 1972: First-order theory and analysis of MF/HF/VHF scatter from the sea. *IEEE Trans. Antennas Propag.*, **20**, 2–10, https://doi.org/10.1109/TAP.1972.1140123.

——, and B. L. Weber, 1977: On the nonlinear theory for gravity waves on the ocean's surface. Part II: Interpretation and applications. *J. Phys. Oceanogr.*, **7**, 11–21, https://doi.org/10.1175/1520-0485(1977)007<0011:OTNTFG>2.0.CO;2.

——, and B. J. Lipa, 1997: Evolution of bearing determination in HF current mapping radars. *Oceanography*, **10**(2), 72–75, https://doi.org/10.5670/oceanog.1997.27.

——, and ——, 1999: Radar angle determination with music direction finding. U.S. Patent 5 990 834.

——, ——, P. M. Lilleboe, and J. Isaacson, 1994: Gated FMCW DF radar and signal processing for range/Doppler/angle determination. U.S. Patent 5 361 072.

Bellomo, L., and Coauthors, 2015: Toward an integrated HF radar network in the Mediterranean Sea to improve search and rescue and oil spill response: The TOSCA project experience. *J. Oper. Oceanogr.*, **8**, 95–107, https://doi.org/10.1080/1755876X.2015.1087184.

Blanton, B. O., and Coauthors, 2004: Barotropic tides in the South Atlantic Bight. *J. Geophys. Res.*, **109**, C12024, https://doi.org/10.1029/2004JC002455.

Bushnell, M., R. Heitsenrether, J. Thomas, C. Galvarino, E. Burger, J. Dorton, and L. Leonard, 2018: Status and near-term plans for the U.S. IOOS Quality Assurance/Quality Control of Real-time Oceanographic Data (QARTOD) project. *OCEANS 2018 MTS/IEEE Charleston*, Charleston, SC, IEEE, https://doi.org/10.1109/OCEANS.2018.8604787.

Cahl, D., and G. Voulgaris, 2016: Beam forming HF radar beam pattern measurements and phase offset calibration using a UAV. *2016 Fall Meeting*, San Francisco, CA, Amer. Geophys. Union, Abstract OS13B-1810, https://agu.confex.com/agu/fm16/meetingapp.cgi/Paper/149833.

——, and ——, 2022: HFcur_BBM: A MATLAB package for calculating surface currents from HF radars using beamforming, Beamscan (direction finding using beamforming) and MUSIC for a linear array. Zenodo, https://doi.org/10.5281/zenodo.7230998.

Chapman, R. D., L. K. Shay, H. C. Graber, J. B. Edson, A. Karachintsev, C. L. Trump, and D. B. Ross, 1997: On the accuracy of HF radar surface current measurements: Intercomparisons with ship-based sensors. *J. Geophys. Res.*, **102**, 18 737–18 748, https://doi.org/10.1029/97JC00049.

Cosoli, S., and S. de Vos, 2019: Interoperability of direction-finding and beam-forming high-frequency radar systems: An example from the Australian high-frequency ocean radar network. *Remote Sens.*, **11**, 291, https://doi.org/10.3390/rs11030291.

Couvelard, X., C. Messager, P. Penven, S. Smet, and P. Lattes, 2021: Benefits of radar-derived surface current assimilation for south of Africa ocean circulation. *Geosci. Lett.*, **8**, 5, https://doi.org/10.1186/s40562-021-00174-y.

Crombie, D. D., 1955: Doppler spectrum of sea echo at 13.56 Mc./s. *Nature*, **175**, 681–682, https://doi.org/10.1038/175681a0.

Dumas, D., and C.-A. Guérin, 2020: Self-calibration and antenna grouping for bistatic oceanographic high-frequency radars. arXiv, 2005.10528v1, https://doi.org/10.48550/arXiv.2005.10528.

Emery, B. M., 2020: Evaluation of alternative direction-of-arrival methods for oceanographic HF radars. *IEEE J. Oceanic Eng.*, **45**, 990–1003, https://doi.org/10.1109/JOE.2019.2914537.

——, L. Washburn, and J. A. Harlan, 2004: Evaluating radial current measurements from CODAR high-frequency radars with moored current meters. *J. Atmos. Oceanic Technol.*, **21**, 1259–1271, https://doi.org/10.1175/1520-0426(2004)021<1259:ERCMFC>2.0.CO;2.

Essen, H.-H., K.-W. Gurgel, and T. Schlick, 2000: On the accuracy of current measurements by means of HF radar. *IEEE J. Oceanic Eng.*, **25**, 472–480, https://doi.org/10.1109/48.895354.

Fernandez, D. M., and J. D. Paduan, 1996: Simultaneous CODAR and OSCR measurements of ocean surface currents in Monterey Bay. *Int. Geoscience and Remote Sensing Symp.*, Lincoln, NE, IEEE, 1749–1752, https://doi.org/10.1109/IGARSS.1996.516789.

Guérin, C.-A., D. Dumas, A. Molcard, C. Quentin, B. Zakardjian, A. Gramoullé, and M. Berta, 2021: High-frequency radar measurements with CODAR in the region of Nice: Improved calibration and performance. *J. Atmos. Oceanic Technol.*, **38**, 2003–2016, https://doi.org/10.1175/JTECH-D-21-0058.1.

Gupta, P., and S. P. Kar, 2015: MUSIC and improved MUSIC algorithm to estimate direction of arrival. *2015 Int. Conf. on Communications and Signal Processing*, Melmaruvathur, India, IEEE, 757–761, https://doi.org/10.1109/ICCSP.2015.7322593.

Gurgel, K.-W., G. Antonischki, H.-H. Essen, and T. Schlick, 1999a: Wellen radar (WERA): A new ground-wave HF radar for ocean remote sensing. *Coastal Eng.*, **37**, 219–234, https://doi.org/10.1016/S0378-3839(99)00027-7.

——, H.-H. Essen, and S. P. Kingsley, 1999b: High-frequency radars: Physical limitations and recent developments. *Coastal Eng.*, **37**, 201–218, https://doi.org/10.1016/S0378-3839(99)00026-5.

Gutierrez, B. T., 2006: Influence of coastal and nearshore morphology on sedimentation and inner shelf circulation. Ph.D. dissertation, University of South Carolina, 185 pp.

Harlan, J., E. Terrill, L. Hazard, C. Keen, D. Barrick, C. Whelan, S. Howden, and J. Kohut, 2010: The Integrated Ocean Observing System high-frequency radar network: Status and local, regional, and national applications. *Mar. Technol. Soc. J.*, **44**, 122–132, https://doi.org/10.4031/MTSJ.44.6.6.

——, and Coauthors, 2011: National IOOS high frequency radar search and rescue project. *OCEANS'11 MTS*, Waikoloa, HI, IEEE, https://doi.org/10.23919/OCEANS.2011.6107090.

Helzel, T., and M. Kniephoff, 2010: Software beam forming for ocean radar WERA features and accuracy. *OCEANS 2010 MTS*, Seattle, WA, IEEE, https://doi.org/10.1109/OCEANS.2010.5664374.

Heron, M. L., 2017: The effect of HF radar beam patterns on surface current and wind direction measurements. *OCEANS 2017*, Aberdeen, United Kingdom, IEEE, https://doi.org/10.1109/OCEANSE.2017.8084849.

Hildebrand, P. H., and R. S. Sekhon, 1974: Objective determination of the noise level in Doppler spectra. *J. Appl. Meteor.*, **13**, 808–811, https://doi.org/10.1175/1520-0450(1974)013<0808:ODOTNL>2.0.CO;2.

Justusson, B. I., 1981: Median filtering: Statistical properties. *Two-Dimensional Digital Signal Processing II: Transforms and Median Filters*, T. S. Huang, Ed., Topics in Applied Physics, Vol. 43, Springer, 161–196.

Kirincich, A., B. Emery, L. Washburn, and P. Flament, 2019: Improving surface current resolution using direction finding algorithms for multiantenna high-frequency radars. *J. Atmos. Oceanic Technol.*, **36**, 1997–2014, https://doi.org/10.1175/JTECH-D-19-0029.1.

Kohut, J. T., and S. M. Glenn, 2003: Improving HF radar surface current measurements with measured antenna beam patterns. *J. Atmos. Oceanic Technol.*, **20**, 1303–1316, https://doi.org/10.1175/1520-0426(2003)020<1303:IHRSCM>2.0.CO;2.

Krim, H., and M. Viberg, 1996: Two decades of array signal processing research: The parametric approach. *IEEE Signal Processes Mag.*, **13**, 67–94, https://doi.org/10.1109/79.526899.

Kuang, L., A. F. Blumberg, and N. Georgas, 2012: Assessing the fidelity of surface currents from a coastal ocean model and HF radar using drifting buoys in the Middle Atlantic Bight. *Ocean Dyn.*, **62**, 1229–1243, https://doi.org/10.1007/s10236-012-0556-2.

Lai, Y., H. Zhou, Y. Zeng, and B. Wen, 2017: Quantifying and reducing the DOA estimation error resulting from antenna pattern deviation for direction-finding HF radar. *Remote Sens.*, **9**, 1285, https://doi.org/10.3390/rs9121285.

Laws, K. E., D. M. Fernandez, and J. D. Paduan, 2000: Simulation-based evaluations of HF radar ocean current algorithms. *IEEE J. Oceanic Eng.*, **25**, 481–491, https://doi.org/10.1109/48.895355.

Lipa, B., B. Nyden, D. S. Ullman, and E. Terrill, 2006: SeaSonde radial velocities: Derivation and internal consistency. *IEEE J. Oceanic Eng.*, **31**, 850–861, https://doi.org/10.1109/JOE.2006.886104.

Liu, Y., R. H. Weisberg, and C. R. Merz, 2014: Assessment of CODAR SeaSonde and WERA HF radars in mapping surface currents on the West Florida shelf. *J. Atmos. Oceanic Technol.*, **31**, 1363–1382, https://doi.org/10.1175/JTECH-D-13-00107.1.

Longuet-Higgins, M. S., 1962: The directional spectrum of ocean waves, and processes of wave generation. *Proc. Roy. Soc. London*, **265A**, 286–315, https://doi.org/10.1098/rspa.1962.0010.

Lorente, P., and Coauthors, 2022: Coastal high-frequency radars in the Mediterranean—Part 1: Status of operations and a framework for future development. *Ocean Sci.*, **18**, 761–795, https://doi.org/10.5194/os-18-761-2022.

MathWorks, 2022: Phased Array System Toolbox: Design and simulate sensor array and beamforming systems. MathWorks, https://mathworks.com/products/phased-array.html.

Paduan, J. D., and I. Shulman, 2004: HF radar data assimilation in the Monterey Bay area. *J. Geophys. Res.*, **109**, C07S09, https://doi.org/10.1029/2003JC001949.

——, and L. Washburn, 2013: High-frequency radar observations of ocean surface currents. *Annu. Rev. Mar. Sci.*, **5**, 115–136, https://doi.org/10.1146/annurev-marine-121211-172315.

Pawlowicz, R., B. Beardsley, and S. Lentz, 2002: Classical tidal harmonic analysis including error estimates in MATLAB using T_TIDE. *Comput. Geosci.*, **28**, 929–937, https://doi.org/10.1016/S0098-3004(02)00013-4.

Read, W., 1989: Review of conventional tactical radio direction finding systems. Defence Research Establishment Ottawa Tech. Note 89-12, 54 pp., https://apps.dtic.mil/sti/pdfs/ADA212747.pdf.

Roarty, H., and Coauthors, 2019: The Global High Frequency Radar Network. *Front. Mar. Sci.*, **6**, 164, https://doi.org/10.3389/fmars.2019.00164.

Schmidt, R., 1986: Multiple emitter location and signal parameter estimation. *IEEE Trans. Antennas Propag.*, **34**, 276–280, https://doi.org/10.1109/TAP.1986.1143830.

Sentchev, A., and Coauthors, 2013: Surface circulation in the Iroise Sea (W. Brittany) from high resolution HF radar mapping. *J. Mar. Syst.*, **109–110**, S153–S168, https://doi.org/10.1016/j.jmarsys.2011.11.024.

Shen, W., K.-W. Gurgel, G. Voulgaris, T. Schlick, and D. Stammer, 2012: Wind-speed inversion from HF radar first-order backscatter signal. *Ocean Dyn.*, **62**, 105–121, https://doi.org/10.1007/s10236-011-0465-9.

Stewart, R. H., and J. W. Joy, 1974: HF radio measurements of surface currents. *Deep-Sea Res. Oceanogr. Abstr.*, **21**, 1039–1049, https://doi.org/10.1016/0011-7471(74)90066-7.

Sun, Y., J. Chen, C. Yuen, and S. Rahardja, 2018: Indoor sound source localization with probabilistic neural network. *IEEE Trans. Ind. Electron.*, **65**, 6403–6413, https://doi.org/10.1109/TIE.2017.2786219.

Szpilka, C., K. Dresback, R. Kolar, J. Feyen, and J. Wang, 2016: Improvements for the western North Atlantic, Caribbean and Gulf of Mexico ADCIRC tidal database (EC2015). *J. Mar. Sci. Eng.*, **4**, 72, https://doi.org/10.3390/jmse4040072.

Taylor, K. E., 2001: Summarizing multiple aspects of model performance in a single diagram. *J. Geophys. Res.*, **106**, 7183–7192, https://doi.org/10.1029/2000JD900719.

Tuncer, T. E., and B. Friedlander, 2009: *Classical and Modern Direction-of-Arrival Estimation*. 1st ed. Academic Press, 456 pp., https://doi.org/10.1016/C2009-0-19135-3.

Van Trees, H. L., 2004: *Optimum Array Processing: Part IV of Detection, Estimation, and Modulation Theory*. John Wiley and Sons, 1472 pp., https://doi.org/10.1002/0471221104.

Viberg, M., B. Ottersten, and T. Kailath, 1991: Detection and estimation in sensor arrays using weighted subspace fitting. *IEEE Trans. Signal Process.*, **39**, 2436–2449, https://doi.org/10.1109/78.97999.

Voulgaris, G., and D. Cahl, 2020: matWERA: A MATLAB package for reading binary data files recorded by a Wellen-Radar (WERA) HF radar. (V.1.0.1). Zenodo, https://doi.org/10.5281/zenodo.3603518.

——, B. K. Haus, P. Work, L. K. Shay, H. E. Seim, R. H. Weisberg, and J. R. Nelson, 2008: Waves initiative within SEACOOS. *Mar. Technol. Soc. J.*, **42**, 68–80, https://doi.org/10.4031/002533208786842507.

——, N. Kumar, K.-W. Gurgel, J. C. Warner, and J. H. List, 2011: 2-D inner-shelf current observations from a single VHF Wellen radar (WERA) station. *2011 IEEE/OES 10th Current, Waves and Turbulence Measurements*, Monterey, CA, IEEE, 57–65, https://doi.org/10.1109/CWTM.2011.5759525.

Wang, W., and E. W. Gill, 2016: Evaluation of beamforming and direction finding for a phased array HF ocean current radar. *J. Atmos. Oceanic Technol.*, **33**, 2599–2613, https://doi.org/10.1175/JTECH-D-15-0181.1.

——, P. Forget, and C. Guan, 2014: Inversion of swell frequency from a 1-year HF radar dataset collected in Brittany (France). *Ocean Dyn.*, **64**, 1447–1456, https://doi.org/10.1007/s10236-014-0759-9.

Wu, X., G. Voulgaris, and N. Kumar, 2017: Parameterization of synoptic weather systems in the South Atlantic Bight for modeling applications. *Ocean Dyn.*, **67**, 1231–1249, https://doi.org/10.1007/s10236-017-1084-x.

——, ——, and ——, 2018: Shelf cross-shore flows under storm-driven conditions: Role of stratification, shoreline orientation, and bathymetry. *J. Phys. Oceanogr.*, **48**, 2533–2553, https://doi.org/10.1175/JPO-D-17-0090.1.

Zhang, J., J. Walsh, and E. W. Gill, 2012: Inherent limitations in high-frequency radar remote sensing based on Bragg scattering from the ocean surface. *IEEE J. Oceanic Eng.*, **37**, 395–406, https://doi.org/10.1109/JOE.2012.2198932.